Direct comparison of time-resolved Terahertz spectroscopy and Hall Van der Pauw methods for measurement of carrier conductivity and mobility in bulk semiconductors

Brian G. Alberding[1], **W. Robert Thurber**[2], and **Edwin J. Heilweil**[1,*]

[1]Radiation Physics Division, National Institute of Standards and Technology, Gaithersburg, MD, 20899, USA

[2]Engineering Physics Division, National Institute of Standards and Technology, Gaithersburg, MD, 20899, USA

Abstract

Charge carrier conductivity and mobility for various semiconductor wafers and crystals were measured by ultrafast above bandgap, optically excited Time-Resolved Terahertz Spectroscopy (TRTS) and Hall Van der Pauw contact methods to directly compare these approaches and validate the use of the non-contact optical approach for future materials and *in-situ* device analyses. Undoped and doped silicon (Si) wafers with resistances varying over six orders of magnitude were selected as model systems since contact Hall measurements are reliably made on this material. Conductivity and mobility obtained at room temperature by terahertz transmission and TRTS methods yields the sum of electron and hole mobility which agree very well with either directly measured or literature values for corresponding atomic and photo-doping densities. Careful evaluation of the optically-generated TRTS frequency-dependent conductivity also shows it is dominated by induced free-carrier absorption rather than small probe pulse phase shifts, which is commonly ascribed to changes in the complex conductivity from sample morphology and evaluation of carrier mobility by applying Drude scattering models. Thus, in this work, the real-valued, frequency-averaged conductivity was used to extract sample mobility without application of models. Examinations of germanium (Ge), gallium arsenide (GaAs), gallium phosphide (GaP) and zinc telluride (ZnTe) samples were also made to demonstrate the general applicability of the TRTS method, even for materials that do not reliably make good contacts (e.g., GaAs, GaP, ZnTe). For these cases, values for the sum of the electron and hole mobility also compare very favorably to measured or available published data.

1. Introduction

The measurement of material properties which relate to conductivity and charge carrier mobility following photoexcitation is vitally important to development of new materials for opto-electronic and photovoltaic applications. Terahertz (THz) spectroscopy is a suitable tool for determining these properties and has been used to study an array of metallic and semiconductor materials [1–10]. In particular, it is a non-contact, all optical method which

*Corresponding author: edwin.heilweil@nist.gov.

offers high throughput evaluation of materials without the need for complete device fabrication and can follow carrier dynamics over a wide range of time scales (picoseconds to nanoseconds or longer). In contrast, more conventional electrical contact measurements are limited to long-time processes which occur over the micrometer or longer length scale and are sensitive to grain boundaries and interfacial effects [11]. Furthermore, it may be difficult to make near zero resistance contact to all materials of interest to extract accurate values for the conductivity and mobility [12]. Despite the many advantages of THz spectroscopy, there are still some misunderstood concepts surrounding this technique which limits its more widespread application to solve current problems in the design and measurement of alternative materials for photoconductive applications.

The major aspect of THz spectroscopy which permits it to probe free carrier conductivity is that the time-dependent electric field of a transmitted THz pulse is directly measured (a.k.a. Terahertz Time-Domain Spectrosocpy, THz-TDS). Both the amplitude and phase of the pulsed THz radiation incident upon, $E_i(t)$, and transmitted through, $E_0(t)$, the sample is obtained as depicted in Figure 1. Fast Fourier Transform (FFT) gives the real, $\sigma_1(\omega)$, and imaginary, $\sigma_2(\omega)$, parts of the frequency-dependent complex-valued conductivity, $\hat{\sigma}(\omega)$, through the absorption coefficient, $\alpha(\omega)$, index of refraction, $n(\omega)$, and permittivity, $\hat{\varepsilon}(\omega)$. Extracting $\hat{\sigma}(\omega)$ by this approach typically allows determination of the charge carrier mobility, μ, through fitting of the spectra to Drude or modified Drude conductivity models, effective medium theory, or local oscillator models [13–15], where choice of fitting model depends on the shape and sign of the $\hat{\sigma}(\omega)$ spectra. These same principles can be applied to samples following photoexcitation (Time-resolved Terahertz Spectroscopy, TRTS), where it is common to directly measure differential changes of the transmitted THz electric field, $\Delta E(t) = E_p(t) - E_0(t)$ ($E_p(t)$ is the THz electric field transmitted through the photoexcited sample). In order to measure $n(\omega)$, accurate measurement of the phase delay is required in order to determine the important material parameters relating to charge carrier density, N, and mobility, μ, and this can be difficult, especially in the situation of small phase delay [16,17].

One simplification occurs when a sample falls within the thin film approximation, where the sample thickness (e.g., <10 μm) is much smaller than the wavelength of THz probe radiation (e.g., 300 μm) [13,18,19]. Under these conditions a phase delay is therefore expected to be negligible. For a thin film on an insulating substrate, the THz transmission through the sample, $\hat{T}_s(\omega)$, relative to that through the bare substrate, $\hat{T}_{sub}(\omega)$, is proportional to the thin film conductivity according to equation (1):

$$\frac{\hat{T}_s(\omega)}{\hat{T}_{sub}(\omega)} = \frac{\hat{E}_s(\omega)}{\hat{E}_{sub}(\omega)} = \frac{1+n_{sub}}{1+n_{sub}+Z_0 d\hat{\sigma}(\omega)}, \quad (1)$$

where, Z_0 is the free space impedance, d is the thin film thickness, n_{sub} is the substrate index of refraction, $\hat{\sigma}(\omega)$ is the complex-valued frequency-dependent conductivity, and $\hat{E}_s(\omega)$ and $\hat{E}_{sub}(\omega)$ are the Fourier Transforms of the time-dependent THz electric field waveforms transmitted through the sample and substrate, respectively. This expression can be

rearranged to give an expression for the conductivity and also rewritten for photoexcited samples which display non-zero static conductivity [20].

Despite samples being prepared as thin films or generated as thin films via photoexcitation when the optical penetration depth is much smaller than the overall sample thickness and less than approximately 10 μm [19,32], there are examples where photoexcitation still leads to an apparent phase delay between ΔE and E_0 [21]. This inevitably leads to changes in $\hat{\sigma}(\omega)$, especially affecting $\sigma_2(\omega)$, by the analysis described by equation (1). For example, even a small phase shift on the order of 10 fs to 20 fs can change the sign of $\sigma_2(\omega)$ from positive to negative, which alters the conductivity model chosen to analyze the frequency-dependent data and therefore obscures the values of μ and N which are commonly determined from these fitting routines. Furthermore, it has been suggested that observation of such a phase shift arises from changes to the index of refraction and therefore invalidates use of the thin film approximation [22].

Herein, we show that the thin film approximation can be used to appropriately analyze the TRTS results for bulk semiconductors (such as silicon, gallium arsenide, germanium, zinc telluride, and gallium phosphide), even when a phase-shift is observed in ΔE. We find that the observed phase shift is dominated by transient changes to the absorption spectrum rather than changes in refractive index at lowest possible experimental excitation powers.

Determination of the charge carrier mobility in bulk Si wafers with various intrinsic doping level was made by applying the thin film approximation to the photoexcited samples and using only the real-valued component of the conductivity measured by TRTS and charge carrier density estimated by the experimental excitation conditions (e.g. excitation fluence) without relying on fitting the complex conductivity to Drude models. These methods were validated by directly comparing the charge carrier mobility values determined by TRTS to those obtained using standard Hall Van der Pauw methods on the same samples (where ohmic contact e.g., linear voltage response and near zero resistance is known to be achievable for bulk Silicon (Si) wafers) or by comparison to literature values.

We note that, although TRTS and THz-TDS have been used to study a wide range of materials encompassing various sample morphologies, no known attempts to make direct comparisons between contact probe and optical THz probe methods on the same samples of standard bulk semiconductors have been reported. Furthermore, earlier TRTS studies of bulk semiconductors mainly focused on GaAs [23–25], which is much more difficult to establish reliable electrical contact. To make direct comparison with contact probe measurements, this study focuses mainly on Si samples where ohmic contact was readily achieved. TRTS studies of bulk Si are limited [26], but TRTS studies on nanostructured Si materials have recently been reported [27–30]. Therefore, the study of bulk Si samples is convenient to elucidate misunderstood concepts of THz spectroscopy for two reasons: 1) the origin of an apparent phase delay can be evaluated because the penetration depths using 400 nm and 800 nm excitation places the photoexcited layer well within the thin-film approximation limit, and 2) because ohmic contact is achievable in silicon, reliable comparisons between contact probe and optical THz techniques are feasible. In Discussion section A, we show that the phase shift observed in ΔE arises from changes in the absorption spectrum and not changes

in refractive index. This permits the thin-film approximation to be made and facilitates determination of the conductivity and carrier mobility for comparison to electrical contact probe methods in silicon (section B) and other bulk semiconductors (section C).

2. Experimental Section

A. Materials

Relevant details concerning the bulk semiconductor wafers and crystals used in this study are shown in Table 1. The undoped and lightly-doped silicon (Si) wafers and the germanium (Ge) sample were purchased from University Wafer (UW) whereas the undoped gallium arsenide (GaAs) sample was purchased from Wafer Technology Ltd (WV) [31]. Undoped gallium phosphide (GaP) and zinc telluride (ZnTe) crystals were purchased from Moltech GmbH and Cleveland Crystals, Inc. Highly-doped, thin film Si wafers were purchased from Ultrasil Corporation and consist of a thin device layer (details shown in Table 1) deposited on a 1 micron thick SiO_2 insulating layer supported on a high resistance Si substrate (SOI). For the N-type sample (UD8756), the Si substrate was 500 μm ± 25 μm thick with (1 to 20) Ω·cm resistivity while for the P-type sample (UD9524) the Si substrate was 400 μm ± 10 μm thick with resistivity >10,000 Ω·cm. The device layer thickness of the highly-doped Si samples was chosen to be greater than the tabulated penetration depth at 400 nm (ca. 82 nm; see ref. [32] for Si and other materials). All the Si samples listed in Table 1 were studied by THz spectroscopy and Hall Van der Pauw methods to determine their conductivity as presented in the Results section, below.

B. Terahertz Spectroscopy Methods

The apparatus for terahertz spectroscopy is based on an amplified femtosecond Ti:sapphire kilohertz repetition rate laser system that has been previously described in detail [33]. Briefly, the amplified 800 nm output is split into three arms and used to generate the visible pump, THz probe, and gated electro-optic detection. This system was used for both static THz-TDS (visible pump beam blocked) and TRTS measurements (pump pulses at 400 nm and 800 nm with beam diameter ca. 5 mm, ca. 50 fs FWHM pulse duration, and fluence ≈ $1×10^{15}$ photons/cm^2 to $1×10^{18}$ photons/cm^2). Samples were mounted on an aperture in a purged dry air box at room temperature. For THz-TDS, electric-field waveforms transmitted through the unexcited sample, $E_0(t)$, and reference, $E_i(t)$ were scanned 10 times and averaged. This averaging scheme typically results in waveforms with a reproducible measured phase delay of ± 5 fs or less. For TRTS measurements, the pump delay was scanned while holding the delay between the gate and THz probe pulses fixed at the position that gives the maximum differential electro-optic response (ΔE) to yield the TRTS decay dynamics. The pump delay scans were again collected 10 times, averaged, and then used to calculate the pump-induced change in conductivity. Spectral changes to the photoconductivity were also determined by measuring the differential electric-field waveforms, ΔE(t), where the delay time between the THz probe and gate is scanned and the delay between the visible pump and THz probe is fixed. Ten sweeps of the differential electric field waveforms were collected, averaged, and used to determine the frequency dependent absorbance and photoconductivity. Fourier transforms of the electric field waveforms were performed. All averaged waveforms were used for data analysis after

acquiring signal sweeps without error analysis (waveforms and derived frequency-dependent conductivity and mobility values for each sample show typical amplitude scatter of a few percent).

C. THz Experimental Data Analysis

Conductivity of the non-photoexcited samples (σ^{np}) was determined in one of two ways depending on the sample. First, for the highly doped thin-film silicon samples (UD8756 and UD9524), conductivity was determined using equation (1) where the undoped silicon sample (UW2018) was used as the comparative substrate. A second method was used for the remaining samples which do not fall within the thin film limit for *static* THz-TDS measurements. In this case, the THz refractive index, n, and absorption coefficient, α, (corrected for reflective losses by the Fresnel equation) were determined relative to air. The real part of the conductivity (σ_1) was then determined from the imaginary permittivity according to $\sigma_1 = \varepsilon_2\varepsilon_0\omega = 2n_s k\varepsilon_0\omega$, where $k = c\alpha/2\omega$, c is the speed of light, and ω is the angular frequency. These conductivity values were compared to contact resistivity measurements and used for determining the change in conductivity following photoexcitation.

For photoexcited samples, conductivity (via TRTS) was determined by analyzing the measured electric field waveforms or ΔE (peak) values under the thin film approximation using modifications of equation (1). The electric field transmission through a sample consisting of a photoexcited layer smaller than the overall sample thickness relative to an unphotoexcited sample is given by:

$$\frac{\hat{T}_s^p(\omega)}{\hat{T}_s^{np}(\omega)} = \frac{\hat{E}_s^p(\omega)}{\hat{E}_s^{np}(\omega)} = \frac{1+n_{\text{sub}}+Z_0 d^{np}\hat{\sigma}^{np}(\omega)}{1+n_{\text{sub}}+Z_0 d^p\hat{\sigma}^p(\omega)}, \quad (2)$$

where the substrate is defined as the unexcited portion of the sample and the superscripts *np* and *p* indicate the non-photoexcited and photoexcited samples, respectively. Equation (2) can be rearranged to give an expression for the conductivity of the photoexcited sample, equation (3).

$$\hat{\sigma}^p(\omega) = \frac{d^{np}\hat{\sigma}^{np}(\omega)}{d^p}\left(\frac{\hat{E}_s^{np}(\omega)}{\Delta\hat{E}(\omega)+\hat{E}_s^{np}(\omega)}\right) - \left(\frac{1+n_{\text{sub}}}{Z_0 d^p}\right)\left(\frac{\Delta\hat{E}(\omega)}{\Delta\hat{E}(\omega)+\hat{E}_s^{np}(\omega)}\right). \quad (3)$$

Equation (3) describes the conductivity determined from the frequency domain electric field, which is determined by Fourier transform of the measured time-dependent electric field. Alternatively, it is also common to take ΔE and E_0 at the peak of the time-dependent electric field[13]. In this latter case, substitution of ΔE(t=peak) and E_0(t=peak) into equation (3) generates the frequency averaged values of the *real* conductivity, which is a good approximation of the DC conductivity when the conductivity spectrum is dispersive.. This equation reduces to previously published forms under the typical approximations that $\hat{\sigma}^{np}(\omega)$ = 0 for an undoped semiconductor and $\Delta E << \hat{E}_s^{np}(\omega)$ at low excitation power [13–18].

However, some important points about this analysis should be noted. First, the carrier concentration resulting from photoexcitation is a function of depth within the sample (Beer's Law exponential fall-off). By using $1/\alpha$ as the penetration depth for the film thickness, the analysis crudely integrates over the depth profile. Second, for the purposes of calculating σ^p, only σ^{np} within the depth of the photoexcited layer should be considered because the changes resulting from photoexcitation only occur within this relatively thin layer (i.e. in equation (3), $d^{np} = d^p$). This analysis was used to determine the frequency-dependent and time-dependent conductivity of all photoexcited samples.

The real part of the conductivity determined by equation (3) is related to the direct current conductivity in the low frequency limit by $\sigma = eN\mu$, where N and μ are the charge carrier density and mobility, respectively, and e is the electron charge. In general, bulk semiconductors such as the ones studied here, generate equal numbers of both electrons and holes with unit quantum yield following photoexcitation so the conductivity is given by a sum of the electron and hole contributions. If the sample is doped, there is an additional term for the intrinsic charge carriers such that:

$$\sigma^p = e\left(N_{e/h}^{\mathrm{np}}\mu_{e/h}^{\mathrm{np}} + N_e^p\mu_e^p + N_h^p\mu_h^p\right), \quad (4)$$

where again, the superscripts p and np represent the photoexcited and non-photoexcited sample and the subscripts e and h represent the electrons or holes in N- or P-type doped materials, respectively, or that result from photoexcitation. In TRTS, the changes in conductivity resulting from photoexcitation are measured directly so for both doped and undoped samples the differential conductivity $\Delta\sigma$, is

$$\Delta\sigma = e\Delta N(\mu_e + \mu_h). \quad (5)$$

$\Delta\sigma$ is determined from THz-TDS using equation (1), and the photoinduced conductivity via TRTS using equation (3). Values for ΔN are determined from the experimental excitation fluence in TRTS (corrected for reflective losses of the excitation pulse by the Fresnel equation) and values for the penetration depth at the excitation wavelength employed [34]. This analysis method therefore provides the sum of the electron and hole mobility in the photoexcited sample regardless of the intrinsic carrier type present. Comparisons of mobility values determined in this way by THz spectroscopy were made directly to Hall van der Pauw measurements on the same samples or to literature values obtained by electrical contact probe methods at room temperature and, where possible, from results for samples of equivalent carrier concentrations. Uncertainty limits for reported mobility values from TRTS measurements were obtained by averaging up to five values for varying excitation fluences and photo-doping levels (k=1 type B uncertainty analysis).

D. Hall Van der Pauw Measurements

The free carrier concentration and mobility for each Si sample was determined by the Hall method with the Van Der Pauw geometry at 295 K and a magnetic field of 0.5 Tesla

(undoped or lightly doped samples) or 0.8 Tesla (for heavily doped samples). For each sample the contact metal was indium and for the highly doped samples the normal soldering contact process was used while for lightly doped and undoped samples the untrasonic soldering process was used. Results were also obtained for Ge and ZnTe with an applied magnetic field of 0.5 Tesla. The contact metal was again indium and normal soldering was used but for ZnTe it required a very hot iron for a longer than average time to achieve satisfactory contact. Similar methods were attempted for GaAs samples but ohmic contact (linear and near zero resistance) was not achieved thereby prohibiting reliable results and direct comparison.

3. Results and Discussion

A. TRTS of undoped semiconductors

TRTS results following 400 nm excitation (at $\approx$ 1 mJ/cm^2) of a high resistivity (> 10 000 $\Omega\cdot$cm) Si wafer are shown in Figure 2. The measured E_0 and ΔE waveforms at various pump delay times are shown in Fig. 2(a). The ΔE waveforms have been scaled by the indicated factor for visual aid. Decay dynamics measured at the peak of ΔE as a fraction of the E_0 transmission are shown in Fig. 2(b) which are flat over the initial 200 ps due to the long lifetime of this indirect band gap bulk semiconductor [34].

It is immediately apparent that photoexcitation leads to a significant phase shift in ΔE compared to E_0 at all pump delay times. This observation is unexpected given that the tabulated penetration depth at 400 nm in Si is only 82 nm [32], which suggests the photoexcited layer in the 280 μm thick Si wafer should be considered as a thin film.

We surmise the observed phase shift is neither solely due to or dominated by changes in real refractive index for two reasons. First, the actual THz waveforms transmitted through the photo-excited sample, obtained by $E_p = \Delta E + E_0$, do not reflect the same phase shift as ΔE, as shown in Figure 2(c). A true phase shift due solely to a change in the real refractive index should be accompanied by much larger changes in ΔE. This situation is indicated in Figure 3 by taking the difference between two identical waveforms with arbitrarily shifted phase and is clearly not reproduced by our measurements. Even a phase shift as small as 0.01 ps (10 fs) would cause large deviations in ΔE to the level of a 9 % change between the values of E_0(peak) and ΔE (peak), again with no magnitude changes between E_0 and E_p. The ΔE waveforms shown in Figure 1(a) exhibit only a 2 % change in peak value at our lowest applied excitation power. Furthermore, if the observed phase shift was dominated by changes in refractive index, it should depend on the thickness of the photoexcited layer. The thickness dependence can be tested by using 800 nm excitation, which has a substantially larger penetration depth of $\approx$ 10.5 μm [32]. Despite a factor of 100 increase in penetration depth, the TRTS results with 800 nm excitation at similar excitation power yield essentially the same shifts between the peaks of the ΔE and E_0 waveforms (see Figure 4).

We contend the second reason for the apparent phase shift in ΔE is that it arises from the induced absorption spectrum of the free charge carriers generated by photoexcitation, which is shown in Figure 2(d) for 400 nm excitation and is similar for 800 nm excitation (Figure 5). It is very apparent that the absorbance decreases with increasing frequency, which is in

full agreement with THz-TDS absorption spectra for lightly doped n- and p-type Si and is expected to be similar given our low excitation power [35]. Because the transient absorption intensity is unequal across the frequency range of our THz pulse, it must necessarily induce changes not only in the probe pulse magnitude but also the shape of the THz waveform. These changes are manifested in ΔE by an apparent phase shift, which can arise due to a broadening of the oscillations present as well as changes in the oscillation frequencies present. We therefore attribute the changes in THz transmission measured by ΔE as being dominated by changes in absorption due to free charge carriers in the photoexcited layer.

It should be noted that we also observe the same characteristics in measured ΔE waveforms and absorption spectra for GaAs (see Figure 6), which has been more widely studied by TRTS. Our measurements for GaAs are comparable to previous THz-TDS measurements of lightly doped GaAs [36] and TRTS measurements of undoped GaAs [13,21,23] where changes in phase were often analyzed by applying classical Drude or related (Drude-Smith) models to extract conductivity and mobility from the frequency-dependent imaginary component. It is important to keep in mind that absorption does correspond to changes in refractive index, according to the Kramers-Kronig relation. However, our results suggest that at these levels of small absorption (at most a few percent), the changes in refractive index are negligible and do not generate an observable true phase shift in the THz wave as it travels through the photoexcited layer. Instead, the "phase shift" arises primarily from changes in shape between the THz waveform transmitted by the photoexcited and non-photoexcited samples as further indicated by the relative differences in oscillation patterns between ΔE and E_0 depicted in Figure 4.

If changes in THz transmission indeed predominantly arise from changes in absorption, then there is no reason why the thin film approximation cannot be applied to these systems to directly determine photoconductivity. What are the implications for the free carrier conductivity induced by THz transient absorption and the corresponding phase-shifted transmitted THz waveforms? One implication is that the imaginary component of the complex conductivity will typically be negative, which drastically changes which conductivity model is appropriate and can be applied to the frequency-dependent data to determine carrier parameters such as N and μ.

Analysis of the E_0 and ΔE waveforms at a pump delay of 50 ps using 400 nm and 800 nm excitation at 1 μJ/cm^2 by equation (3) for the undoped Si and GaAs wafers yield the conductivity spectra shown in Figure 7. Here we used the approximation that $\hat{\sigma}^{np}(\omega) = 0$ for undoped semiconductors. For both materials, we find $\sigma_2^p(\omega)$ is, in fact, negative across our detectable frequency range, which suggests non-Drude like behavior and prevents any further analysis by fitting to typical Drude conductivity models. This finding disagrees with previously published TRTS conductivity spectra for GaAs, which reported $\sigma_2(\omega) > 0$, although the shape of $\sigma_1(\omega)$ from our experiments is in very good agreement with the same published spectra [13,21,23] and THz-TDS spectra of lightly doped Si and GaAs [35,36]. We emphasize that the shape of $\sigma_2(\omega)$ reported in the literature is very similar to those extracted from our measurements shown in Figure 7, except that our analysis yields the opposite sign for $\sigma_2(\omega)$.

In order to further justify that the correct sign for $\sigma_2(\omega)$ is negative, we also examined and show the excitation power dependence of the TRTS results in Figure 8 for the undoped GaAs wafer and in Figure 9 for the undoped Si wafer. It is important to keep in mind that in our analysis of the conductivity by equation (3) for undoped Si and GaAs, we assumed $\hat{\sigma}^{np}(\omega) = 0$, which is a common approximation for semiconductors with low intrinsic conductivity [13,18]. We also note that this assumption cannot be correct because a material's real refractive index is non-zero and therefore $\sigma_2^{\mathrm{np}}(\omega) \neq 0$ (see below), but the assumption that $\sigma_2^{\mathrm{np}}(\omega) = 0$ is the prevailing practice in the literature. We can, however, derive the expected sign change of $\sigma_2(\omega)$ under this assumption.

If $\hat{\sigma}^{np}(\omega) = 0$, then the complex conductivity is given by $\hat{\sigma}^p(\omega) = \varepsilon_0 \omega [\varepsilon_2 - i(\varepsilon_1 - 1)]$, where $\varepsilon_2 = 2n^p k^p$, $\varepsilon_1 = (n^p)^2 - (k^p)^2$, and $k^p = c\alpha/4\pi f$ (n^p is the excited sample refractive index, α is the absorption coefficient, c is the speed of light, and f is the THz frequency). In the limit as the sample absorption and therefore k^p goes to zero, $\varepsilon_1 > 1$ (because for pure Si, $N = 3.418$), $\varepsilon_2 = 0$ and therefore $\sigma_2^p(\omega)$ must be negative, which agrees with our observations at low excitation power. The E_p waveforms shown in Fig. 9(a) indicate the index of refraction, n^p, is not strongly changed by excitation at powers ranging from (1 to 100) μJ/cm^2, while Fig. 9(b) shows that, as one would expect, the total absorption increases with power, especially at higher frequency. We thus again contend that the phase changes observed in the measured ΔE waveform shown in Fig. 9(c) are dominated by a transient absorption change and not a true phase delay. This conclusion is also reflected by the observation that the phase of ΔE at high excitation power shifts back towards that of E_0 as the absorption begins to more strongly include higher frequencies within the THz pulse. Most importantly, this final discussion further supports that the observed sign of $\sigma_2^p(\omega)$ is dominated by the transient absorption. The increased absorption eventually leads to $k^p > n^p$ and therefore $\sigma_2^p(\omega)$ trends positive, which is in agreement with our measurements shown in Fig. 9(d).

The problems discussed above associated with determining the sign of $\sigma_2(\omega)$ arise from assumptions made (i.e. that $\hat{\sigma}^{np}(\omega) = 0$) and choice of standard reference (i.e. measuring versus air, undoped semiconductor, etc.) which may not account for phase changes if not accurately determined. Depending on these choices, the sign of $\sigma_2(\omega)$ can change because it depends on the relative magnitudes of the refractive index and absorption. However, the underlying physics which lead to the observed conductivity spectra should not be dependent upon such choices if meaningful properties about charge carrier transport are to be ascribed according to the various conductivity models. In our case, we assumed $\hat{\sigma}^{np}(\omega) = 0$ in equation (3) for the undoped semiconductors, which is valid only for the real part of the conductivity and explains why $\sigma_1(\omega)$ agrees well with values reported in the literature. For conductive doped semiconductors, this assumption cannot be made but the real part of $\sigma^{np}(\omega)$ can be determined from THz-TDS. In either case, relevant values for conductivity and charge carrier mobility can be determined by using equation (3) and focusing only on the real conductivity, which is outlined in the following sections.

B. TDS and TRTS of insulating and doped Silicon (i.e. Si-FZ vs doped Si samples)

Static measurements of the conductivity for the silicon samples at various doping levels and intrinsic conductivies (spanning ca. 6 orders of magnitude; see Table 1) were made using

THz-TDS and Van der Pauw Hall methods. For the undoped (Float Zone Si-Un-2018) and lightly doped samples with large thicknesses, the real part of the THz-TDS conductivity was directly determined from THz absorption (corrected for reflective losses according to the Fresnel equation) and refractive index (as depicted in Figure 1 and presented in the experimental section). For the undoped Si sample, there was no discernible difference between the THz waveforms transmitted through the sample and air (other than reflected amplitude and phase delay), indicating negligible sample conductivity expected for the low doping level. The thin-film approximation, equation (1), was used to determine the conductivity for the highly doped samples using the undoped silicon sample as the substrate reference. The real conductivity spectra for the four doped samples determined in this way is shown in Figure 10 and the measured conductivity results are summarized in Table 2 with comparison to the Hall Van der Pauw Hall measurements.

It is evident from Table 2 that both methods for the same sample yield conductivity values in agreement to within a factor of at most two. Ideally, the conductivity at zero frequency is equivalent to the DC conductivity measured by contact probe methods. This is approximated by using the lowest frequency value in THz spectroscopy, or equivalently, when the spectra are dispersive (relatively invariant) by averaging over the measured frequency range. As indicated by Table 2, there is order-of-magnitude agreement between optical THz spectroscopy (when using frequency-averaged or the lowest frequency value) and Hall Van der Pauw methods but exact agreement is not necessarily expected. While both contact and optical methods will have their own implicit errors, this level of agreement does suggest optical methods are a viable alternative, especially when contacts are difficult to establish.

Changes in conductivity of these samples following photoexcitation were measured using TRTS. Representative scans of $\Delta E/E_0$ scaled to the excitation power for the undoped, lightly-doped, and highly-doped silicon samples are shown in Figure 11(a) using 400 nm excitation. This wavelength was required to contain the ≈ 82 nm photoexcited material within the thin-film layer of the highly doped samples. The dynamics are flat across the 200 ps time scale of our experiment and are therefore not affected by the intrinsic doping level. More importantly, obvious differences in the signal magnitude are observed between the highly doped and lightly/undoped samples. This is an indication of the differences in charge carrier mobility inherent to each of the samples, where increased carrier scattering occurs at higher doping levels and so the mobility decreases.

It is interesting that the lightly doped samples had nearly equivalent signal levels as the undoped sample, which was true for both 400 nm and 800 nm, Figure 11(b), excitation. This is an indication of the nearly equivalent carrier mobility between the samples. The similarity between the P-type and N-type silicon arises because, (1) the carrier density generated by photoexcitation is larger than the intrinsic carrier density and, (2) photoexcitation generates equal numbers of electrons and holes regardless of the intrinsic doping type. Furthermore, it can be seen that the undoped and lightly doped silicon samples have significantly larger signal magnitudes when excited at 800 nm compared to 400 nm. This indicates the carrier mobility is higher for 800 nm excitation and is consistent with the significantly lower photogenerated carrier density at similar excitation fluence due to the larger penetration depth of 10.7 μm (versus 82 nm for 400 nm excitation) at this pump wavelength.

To gain a clearer picture of the carrier mobility that result from photoexcitation of these samples, equivalent measurements of ΔE/E were made at multiple excitation fluences. The data obtained at each excitation fluence is provided in Table 3. The measured ΔE/E signals exhibit a linear power dependence and carrier mobility values were determined at each fluence according to equations (3) and (5). In order to facilitate comparisons between samples, the results at each fluence were averaged and displayed in Table 4. The trends implied by Figure 11 are confirmed by the mobility values displayed in Table 4: That is, smaller signal levels are observed at a given excitation power for samples with higher carrier density and lower carrier mobility.

We find that the extracted mobility values for the silicon samples studied in this work are consistent with literature values for samples of equivalent dopant type and intrinsic carrier density and the typical dependence of carrier mobility on dopant type and concentration was observed [37–40]. For the TRTS experiments, the carrier density resulting from photoexcitation was significantly different from the intrinsic doping level. No difference in mobility extracted by TRTS was observed between intrinsically P- and N-doped samples because photoexcitation generates equal amounts of electrons and holes. However, the highly doped samples did show comparatively lower mobility due to their much higher intrinsic doping level. Furthermore, the highly doped P-type sample (Si-P-5480) is reported to have ca. 5 times higher intrinsic doping level (Table 2) and therefore slightly smaller mobility than the corresponding highly doped N-type sample.

Because both electrons and holes are generated in equal amounts via photoexcitation, we expect the mobility determined by TRTS displayed in Table 4 to represent the sum of the electron and hole mobility according to equation (5). To verify this, we compare the TRTS experimental values to known literature values for P- and N-type silicon doped at similar levels as that resulting from photoexcitation in our experiment. Using 400 nm excitation, the carrier density resulting from photoexcitation was on the order of 1×10^{17} cm^{-3} and 1×10^{18} cm^{-3} for the lightly doped and heavily doped samples, respectively. For the lightly doped samples, $\Delta N = 1 \times 10^{17}$ cm^{-3} is much greater than the intrinsic doping level of 2×10^{15} cm^{-3} (known from Hall measurement, Table 2) and the carrier density arising from photoexcitation is a good approximation of the total carrier density. The literature carrier mobility for both a phosphorus doped and boron doped silicon wafer with a 1.4×10^{17} cm^{-3} dopant level is 641 cm^2/V·s and 293 cm^2/V·s, respectively. The sum of these electron and hole mobility is 934 cm^2/V·s, which agrees quite well with the value measured by TRTS (averaged over multiple excitation fluences for 400 nm excitation) of 948 ± 73 cm^2/V·s [39]. For the highly doped silicon samples, the excitation density at 400 nm is on the same order of magnitude as the intrinsic doping density. Therefore, the literature mobility values at a doping level equal to the sum of the excitation density plus intrinsic density were considered. Again, the average mobility values determined by TRTS measurement (229 ± 15 cm^2/V·s and 174 ± 22 cm^2/V·s for N and P doping, respectively) agreed well with the sum of the electron and hole mobility from the literature [39]. Similarly, we consider the results for 800 nm excitation for the lightly doped silicon samples, which had similar excitation density on the order of 5×10^{15} cm^{-3} compared to the intrinsic doping level. For these cases, the carrier mobility is higher compared to 400 nm excitation due to the smaller photoexcited

carrier density and again agree well with the sum of the electron and hole mobility from the literature at equivalent carrier density.

C. Using TRTS to extract carrier mobility of other semiconductors

To test and show that the method for determining charge carrier conductivity and mobility values from only the real conductivity (as determined by TRTS) is applicable across various materials (since TRTS signal levels at given experimental conditions differ according to the carrier mobility in each material), measurements were obtained for gallium arsenide, germanium, gallium phosphide and zinc telluride at low intrinsic doping levels for comparison to the silicon results. Static THz-TDS measurements revealed that the THz transmission magnitude was nearly equivalent to a measurement of dry purged air (implying zero THz absorption when corrected for surface reflections in the THz spectral range 0.3 THz to 2.1 THz according to the index of refraction and Fresnel equation) for all the samples except ZnTe. For the ZnTe sample studied, the THz transmission was significantly attenuated and yielded a peak THz absorption at 1.7 THz, in agreement with other THz absorption measurements [41]. This THz-TDS absorption in ZnTe is not likely the result of free charge carriers but a low energy phonon absorption in the THz range (there are two weak absorptions < 2 THz, but the strong optical phonon band is centered at 5 THz). Due to these results, each sample was considered as "lightly doped" with low intrinsic conductivity prior to photoexcitation for the TRTS measurements. This was substantiated for Si-Un(2018), ZnTe, and Ge, by Hall measurements which indicated resistivity of 12 kΩ-cm, 45.3 Ω·cm, and 61.4 Ω·cm, respectively, as shown in Table 5. For the GaAs and GaP crystals, we were unable to make electrical contact, so the THz-TDS measurements indicate static conductivity lower than our detection limit.

Each of the intrinsically low doped semiconductor samples were photoexcited above their band gap transition and changes to the conductivity were monitored by TRTS. As in the previous section, $\Delta E/E_0$ at the peak of each waveform was measured and then scaled to the excitation power. Furthermore, experiments at multiple excitation fluences were carried out and shown to yield a linear power dependent response (See Tables 6 and 7). Figure 12 shows representative pump delay scans of $\Delta E/E_0$ scaled to the incident excitation power for each semiconductor.

The time-dependent changes that occur following photoexcitation are related to changes in the conductivity which result from changes in carrier density, N, and/or mobility, μ (i.e. the $\Delta E/E_0$ scale is proportional to the product of carrier density and mobility according to equation (5)). For materials with short recombination lifetimes, such as direct gap semiconductors like GaAs, significant decays are observed due to a time-dependent reduction in carrier density [40]. Conversely, indirect semiconductors such as Si tend to have longer recombination lifetimes, although initially short (ca. 20 ps) decays were also observed for Ge, ZnTe and GaP on our measured timescale. Exact assignments of decay mechanisms are not the focus of this paper. Therefore, in order to make comparisons of signal level (i.e. carrier mobility), the measured $\Delta E/E_0$ values were evaluated at the peak of the pump-probe delay scans. Determination of the mobility at later pump-probe delay times

depends on the assignment of the decay dynamics to time-dependent changes in N or μ (or both).

For each semiconductor sample, equation (3) was used to determine the change in conductivity following photoexcitation and equation (5) was used to determine the carrier mobility at the peak of each $\Delta E/E_0$ decay. The results were averaged over the entire set of excitation fluences used for each semiconductor sample and are shown in Table 8. In order to make appropriate comparisons of the optical (TRTS) and contact probe (Hall Van der Pauw) techniques, known values for the electron and hole mobility are needed at equivalent carrier densities. As stated before, the carrier concentration dependence of mobility for both electrons and holes is well known for silicon (see above) [37–40] and the values obtained by TRTS agree well with ($\mu_e+\mu_h$) at equivalent carrier densities determined by the contact probe measurements for undoped (and atomically doped) silicon samples.

As presented in Table 8, mobility values obtained for samples other than high resistivity, undoped Si were examined using TRTS and compared to measured sample Hall values or those from the literature. Again, acceptable contacts were only successfully made for the Ge and ZnTe samples. Mobility values obtained from the literature are included as estimates for these materials. We find that for GaAs, when using 400 nm excitation, the TRTS extracted mobility sum (1363 cm^2/V·s) is significantly lower than the literature sum (2850 cm^2/V·s) most likely because the penetration depth for 400 nm is only about 80 nm. When 800 nm excitation is used (ca. 10 μm penetration), significantly better agreement between our measured sum (5555 cm^2/V·s vs the literature sum 5375 cm^2/V·s) is found. Preferred use of 800 nm excitation of GaAs instead of 400 nm to avoid penetration effects has been discussed previously [23,25]. For Ge and GaP samples, very good agreement with measured TRTS and Hall mobility values are found (within experimental errors). Recall that our ZnTe test sample exhibited static THz absorption from low frequency phonon modes or intrinsic residual doping, so the measured TRTS value of 565 ± 103 cm^2/V·s may be difficult to compare to the measured Hall result of 107 ± 5 cm^2/V·s, which is only sensitive to holes. We were unable to locate appropriate literature values for p or n-type samples doped at the minimal photodoping level of 5.1×10^{17} cm^{-3} used in TRTS to directly compare to our measurement. In short, except for the ZnTe sample, we find very reasonable agreement between our TRTS extracted mobility sum values compared to direct Hall measurements (dominated by either electron or hole mobility) on the same samples or compared to the mobility sums available from literature data. This evaluation gives credence to using all-optical THz methods for evaluating conductivity and mobility values when creating ohmic contact is prohibitive or even for evaluating carrier properties of unknown or new semiconductor materials.

4. Conclusions

In this paper we described how to employ static THz-TDS and TRTS methods to make all optical, non-contact measurements of the photoconductivity and charge carrier mobility in bulk semiconductors. The optical measurements were also directly validated based on comparisons to electrical contact measurements, i.e. resistivity and Hall Van der Pauw methods on the same samples, as well as by comparison to cited literature values. The comparisons of the two methods is made by focusing on measurements of Si samples

containing either n-type or p-type doping with concentrations yielding resistivities spanning from 0.01 Ω·cm to 10 000 Ω·cm. Si samples were chosen to make "standards" comparisons because they give the most reliable contact probe measurements due to silicon's known ability to provide ohmic contact. By showing that optical, THz spectroscopy methods give reasonable values compared to Hall Van der Pauw methods, we then also showed that the THz optical methods can be used for differentiating and categorizing other semiconductor materials (for which standard procedures for achieving electrical contact are poor or less well established) in terms of photoconductivity and charge mobility compared to the standard Si reference materials.

We also presented a new interpretation for the origin of previously published complex conductivity sign and frequency dependence. Many literature studies often observe and attribute photo-induced probe pulse phase changes, which sensitively determines the sign of the complex conductivity, to specific mobility and sample scattering properties. Drude and modified Drude models are then applied to extract conductivity values and mobility and ascribe carrier dynamics induced by various material morphologies. Conversely, we showed in this work that the THz waveform pulse merely changes shape due to unequal carrier absorption across the THz spectral range. This results in apparent phase shifts that manifest as artificial changes to the refractive index according to the analysis of equations 1–4, yielding concomitant negative imaginary conductivity and precluding application of the Drude model. Using the model-independent positive real part of the complex conductivity removes these ambiguities and permits direct determination of bulk semiconductor conductivity and measures the total (electron and hole) carrier mobility.

Measurement of conductivity by these optical methods should generally alleviate problems with determining physical means for establishing conductive contact to different samples of interest. In principle, optical spectroscopy offers the possibility of rapid relative carrier properties measurement of different types of samples while holding experimental conditions constant. Furthermore, TRTS offers the opportunity to study individual samples and materials over a wide range of dopant levels simply by controlling the excitation fluence or tuning the excitation wavelength (also by changing thickness to smaller than the penetration depth as long as no morphological changes coincide). This could be an important tool for examining novel materials and actual devices, given the current lack of controlled studies in the literature for dopant concentration dependence of carrier mobility on a wide range of samples.

As demonstrated in this work, TRTS offers a straightforward way to control carrier dopant concentration in individual samples over a wide range of magnitudes simply by changing the excitation fluence and/or wavelength. However, when using optical excitation, there is no way to separate the combined contributions from electrons and holes which are both generated following photoexcitation in TRTS experiments. For THz-TDS measurements there is the possibility of using a magnetic field or monitoring conductivity as a function of sample temperature to identify the presence and/or dominance of electrons or holes, analogous to the Hall Van der Pauw method. The next challenges are to examine potential ways to disentangle these contributions when applying the TRTS method in both transmission and reflection modes.

Acknowledgments

References

1. Beard MC, Turner GM, Schmuttenmaer CA. Terahertz Spectroscopy. J. Phys. Chem. B. 2002; 106(29):7146–7159.

2. Walther M, Cooke DG, Sherstan C, Hajar M, Freeman MR, Hegmann FA. Terahertz Conductivity of Thin Gold Films at the Metal-Insulator Percolation Transition. Phys. Rev. B. 2007; 76(12):125408.

3. van Exter M, Grischkowsky D. Carrier Dynamics of Electrons and Holes in Moderately Doped Silicon. Phys. Rev. B. 1990; 41(17):12140–12149.

4. Ostroverkhova O, Cooke DG, Shcherbyna S, Egerton RF, Hegmann FA, Tykwinski RR, Anthony JE. Bandlike Transport in Pentacene and Functionalized Pentacene Thin Films Revealed by Subpicosecond Transient Photoconductivity Measurements. Phys. Rev. B. 2005; 71(3):035204.

5. Cunningham PD, Hayden LM, Yip H-L, Jen AKY. Charge Carrier Dynamics in Metalated Polymers Investigated by Optical-Pump Terahertz-Probe Spectroscopy. J. Phys. Chem. B. 2009; 113(47): 15427–15432. [PubMed: 19886608]

6. Esenturk O, Melinger JS, Heilweil EJ. Terahertz Mobility Measurements on Poly-3-Hexylthiophene Films: Device Comparison, Molecular Weight, and Film Processing Effects. J. Appl. Phys. 2008; 103(2):023102.

7. Jin Z, Gehrig D, Dyer-Smith C, Heilweil EJ, Laquai F, Bonn M, Turchinovich D. Ultrafast Terahertz Photoconductivity of Photovoltaic Polymer–Fullerene Blends: A Comparative Study Correlated with Photovoltaic Device Performance. J. Phys. Chem. Lett. 2014; 5(21):3662–3668. [PubMed: 26278734]

8. Mihnev MT, Kadi F, Divin CJ, Winzer T, Lee S, Liu C-H, Zhong Z, Berger C, de Heer WA, Malic E, et al. Microscopic Origins of the Terahertz Carrier Relaxation and Cooling Dynamics in Graphene. Nat. Commun. 2016; 7:11617. [PubMed: 27221060]

9. Turner GM, Beard MC, Schmuttenmaer CA. Carrier Localization and Cooling in Dye-Sensitized Nanocrystalline Titanium Dioxide. J. Phys. Chem. B. 2002; 106(45):11716–11719.

10. Alberding BG, Kushto GP, Lane PA, Heilweil EJ. Reduced Photoconductivity Observed by Time-Resolved Terahertz Spectroscopy in Metal Nanofilms with and without Adhesion Layers. Appl. Phys. Lett. 2016; 108(22):223104. [PubMed: 27818524]

11. Kline RJ, McGehee MD. Morphology and Charge Transport in Conjugated Polymers. J. Macromol. Sci. Part C. 2006; 46(1):27–45.

12. Bittle EG, Basham JI, Jackson TN, Jurchescu OD, Gundlach DJ. Mobility Overestimation due to Gated Contacts in Organic Field-Effect Transistors. Nat. Commun. 2016; 7:10908. [PubMed: 26961271]

13. Hegmann, FA., Ostroverkhova, O., Cooke, DG. Photophysics of Molecular Materials. Wiley-VCH: Weinheim; 2006. Probing Organic Semiconductors with Terahertz Pulses; p. 367-428.

14. Ulbricht R, Hendry E, Shan J, Heinz TF, Bonn M. Carrier Dynamics in Semiconductors Studied with Time-Resolved Terahertz Spectroscopy. Rev. Mod. Phys. 2011; 83(2):543–586.

15. Beard MC, Turner GM, Schmuttenmaer CA. Size-Dependent Photoconductivity in CdSe Nanoparticles as Measured by Time-Resolved Terahertz Spectroscopy. Nano Lett. 2002; 2(9):983–987.

16. Kang T-T, Yamamoto M, Tanaka M, Hashimoto A, Yamamoto A, Sudo R, Noda A, Liu DW, Yamamoto K. Terahertz Characterization of Semiconductor Alloy AlInN: Negative Imaginary Conductivity and Its Meaning. Opt. Lett. 2009; 34(16):2507. [PubMed: 19684831]

17. Schneider A. Terahertz Characterization of Semiconductor Alloy AlInN: Negative Imaginary Conductivity and Its Meaning: Comment. Opt. Lett. 2010; 35(2):265. [PubMed: 20081989]

18. Nuss, MC., Orenstein, J. Millimeter and Submillimeter Wave Spectroscopy of Solids. Springer; Berlin: 1998. Terahertz Time-Domain Spectroscopy.

19. Nienhuys H-K, Sundström V. Intrinsic Complications in the Analysis of Optical-Pump, Terahertz Probe Experiments. Phys. Rev. B. 2005; 71(23):235110.

20. Alberding BG, DeSario PA, So CR, Dunkelberger AD, Rolison DR, Owrutsky JC, Heilweil EJ. Static and Time-Resolved Terahertz Measurements of Photoconductivity in Solution-Deposited Ruthenium Dioxide Nanofilms. J. Phys. Chem. C. 2017; 121(7):4037–4044.

21. Cunningham PD. Accessing Terahertz Complex Conductivity Dynamics in the Time-Domain. IEEE Trans. Terahertz Sci. Technol. 2013; 3(4):494–498.

22. Ostroverkhova O, Shcherbyna S, Cooke DG, Egerton RF, Hegmann FA, Tykwinski RR, Parkin SR, Anthony JE. Optical and Transient Photoconductive Properties of Pentacene and Functionalized Pentacene Thin Films: Dependence on Film Morphology. J. Appl. Phys. 2005; 98(3):033701.

23. Beard MC, Turner GM, Schmuttenmaer CA. Transient Photoconductivity in GaAs as Measured by Time-Resolved Terahertz Spectroscopy. Phys. Rev. B. 2000; 62(23):15764–15777.

24. Beard MC, Turner GM, Schmuttenmaer CA. Subpicosecond Carrier Dynamics in Low-Temperature Grown GaAs as Measured by Time-Resolved Terahertz Spectroscopy. J. Appl. Phys. 2001; 90(12):5915–5923.

25. Schall M, Jepsen PU. Photoexcited GaAs Surfaces Studied by Transient Terahertz Time-Domain Spectroscopy. Opt. Lett. 2000; 25(1):13. [PubMed: 18059766]

26. Suzuki T, Shimano R. Time-Resolved Formation of Excitons and Electron-Hole Droplets in Si Studied Using Terahertz Spectroscopy. Phys. Rev. Lett. 2009; 103(5):057401. [PubMed: 19792534]

27. Bergren MR, Palomaki PKB, Neale NR, Furtak TE, Beard MC. Size-Dependent Exciton Formation Dynamics in Colloidal Silicon Quantum Dots. ACS Nano. 2016; 10(2):2316–2323. [PubMed: 26811876]

28. Tang H, Zhu L-G, Zhao L, Zhang X, Shan J, Lee S-T. Carrier Dynamics in Si Nanowires Fabricated by Metal-Assisted Chemical Etching. ACS Nano. 2012; 6(9):7814–7819. [PubMed: 22891641]

29. Fekete L, Kužel P, Němec H, Kadlec F, Dejneka A, Stuchlík J, Fejfar A. Ultrafast Carrier Dynamics in Microcrystalline Silicon Probed by Time-Resolved Terahertz Spectroscopy. Phys. Rev. B. 2009; 79(11):115306.

30. Cooke DG, MacDonald AN, Hryciw A, Meldrum A, Wang J, Li Q, Hegmann FA. Ultrafast Terahertz Conductivity of Photoexcited Nanocrystalline Silicon. J. Mater. Sci. Mater. Electron. 2007; 18(1):447–452.

31. Certain commercial equipment or materials are identified in this paper to adequately specify the experimental procedures. In no case does the identification imply recommendation or endorsement by NIST, nor does it imply that the materials or equipment identified are necessarily the best available for the purpose.

32. Palik, ED., editor. Handbook of Optical Constants of Solids. Academic Press; New York: 1985.

33. Alberding BG, Biacchi AJ, Hight Walker AR, Heilweil EJ. Charge Carrier Dynamics and Mobility Determined by Time-Resolved Terahertz Spectroscopy on Films of Nano-to-Micrometer-Sized Colloidal Tin(II) Monosulfide. J. Phys. Chem. C. 2016; 120(28):15395–15406.

34. Lauer K, Laades A, Übensee H, Metzner H, Lawerenz A. Detailed Analysis of the Microwave-Detected Photoconductance Decay in Crystalline Silicon. J. Appl. Phys. 2008; 104(10):104503.

35. Jeon T-I, Grischkowsky D. Nature of Conduction in Doped Silicon. Phys. Rev. Lett. 1997; 78(6):1106–1109.

36. Katzenellenbogen N, Grischkowsky D. Electrical Characterization to 4 THz of N- and P-type GaAs Using THz Time-domain Spectroscopy. Appl. Phys. Lett. 1992; 61(7):840–842.

37. Thurber WR, Mattis RL, Liu YM, Filliben JJ. Resistivity-Dopant Density Relationship for Phosphorus-Doped Silicon. J. Electrochem. Soc. 1980; 127(8):1807–1812.

38. Thurber WR, Mattis RL, Liu YM, Filliben JJ. Resistivity-Dopant Density Relationship for Boron-Doped Silicon. J. Electrochem. Soc. 1980; 127(10):2291–2294.

39. www.cleanroom.byu.edu/ResistivityCal.phtml.

40. Berger, LI. Semiconductor Materials. CRC Press; Boca Raton, FL: 1997.

41. Tripathi SR, Aoki M, Takeda M, Asahi T, Hosako I, Hiromoto N. Accurate Complex Refractive Index with Standard Deviation of ZnTe Measured by Terahertz Time Domain Spectroscopy. Jpn. J. Appl. Phys. 2013; 52(4R):042401.

42. Rode, DL. Semiconductors and Semimetals. Vol. 10. Academic Press; New York: 1975.

43. Brozel, MR., Stillman, GE. Properties of GaAs. INSPEC, The Institution of Electrical Engineers: London; United Kingdom: 1996.

44. Http://Www.ioffe.ru/SVA/NSM/Semicond/.

45. Fistul VI, Iglitsyn MI, Omelyanovskii EM. Sov Phys Solid State. 1962; 4(4):784–785.

46. Golikova OA, Moizhez BY, Stilbans LS. Sov Phys Solid State. 1962; 3(10):2259–2265.

47. Kao YC, Eknoyan O. Electron and Hole Carrier Mobilities for Liquid Phase Epitaxially Grown GaP in the Temperature Range 200–550 K. J. Appl. Phys. 1983; 54(5):2468–2471.

48. Hishida Y, Ishii H, Toda T, Niina T. Growth and Characterization of MBE-Grown ZnTe:P. J. Cryst. Growth. 1989; 95(1):517–521.
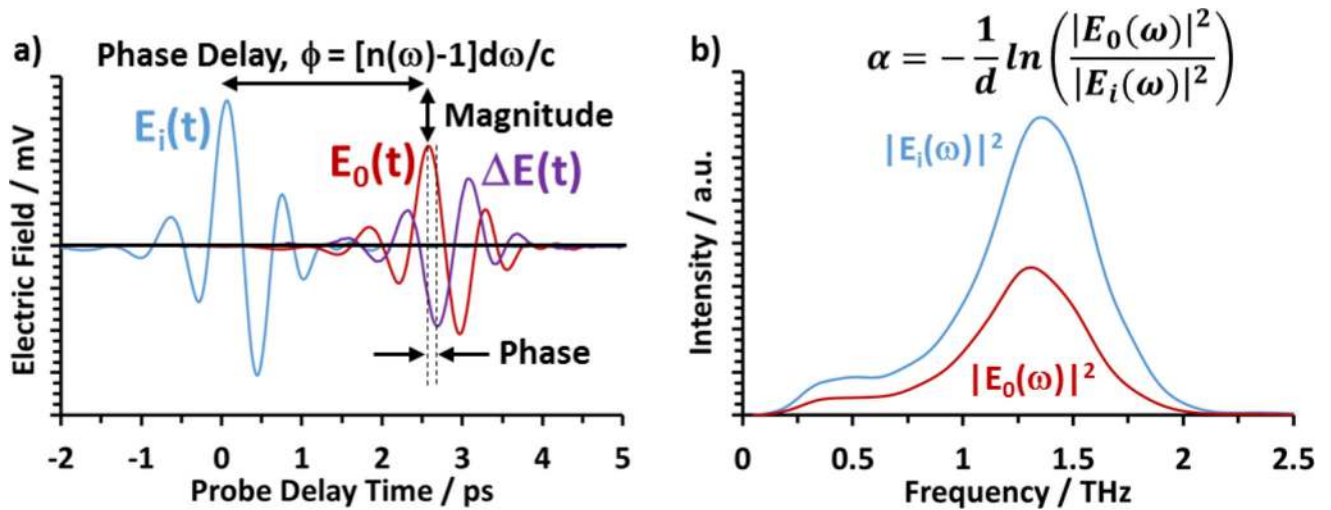
Fig. 1.
Determination of optical parameters such as index of refraction, n, and absorption
coefficient, α, from THz Spectroscopy. (a) Representation of time-domain electric field
waveforms measured by THz-TDS and TRTS. (b) Corresponding frequency-domain
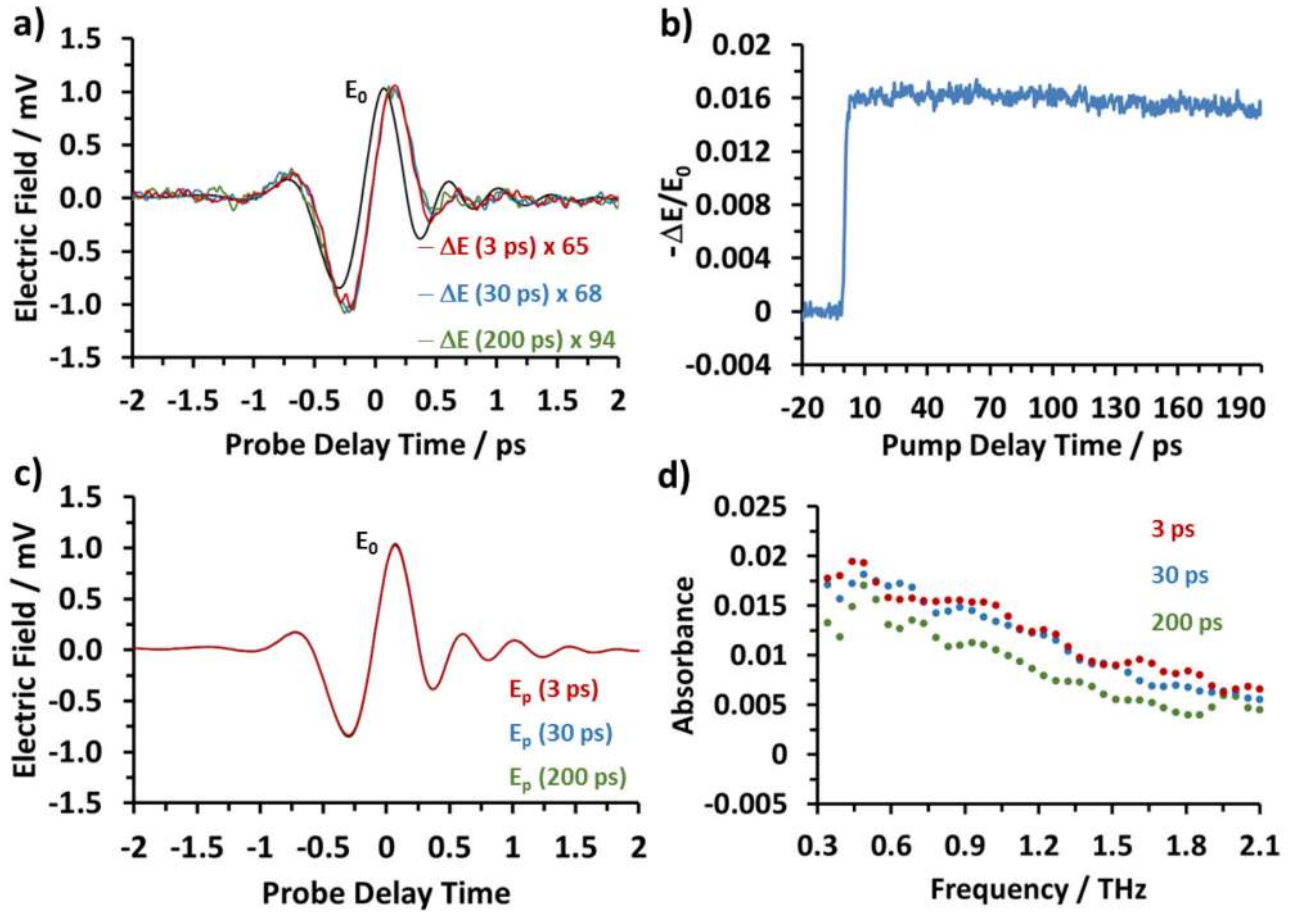intensity spectra obtained from the FFT of $E_i(t)$ and $E_0(t)$.

Fig. 2.
TRTS results for an undoped Si wafer following 400 nm excitation at room temperature. (a) ΔE measured at various pump delay times with 1 $\mu J/cm^2$ pump power and scaled by the indicated factor for aid in comparison to E_0 (black trace) (b) Dynamics measured at the peak of ΔE with 0.6 $\mu J/cm^2$ pump power. (c) THz E-field transmitted through the photoexcited sample determined from $\Delta E = E_p - E_0$. The photoinduced changes are less than 2 % of E_0, and therefore E_p at each delay is basically superimposable with E_0. (d) THz transient absorption spectra determined by ratios of the transmitted probe intensities (see Fig. 1) derived by FFT of the waveforms shown in part c.
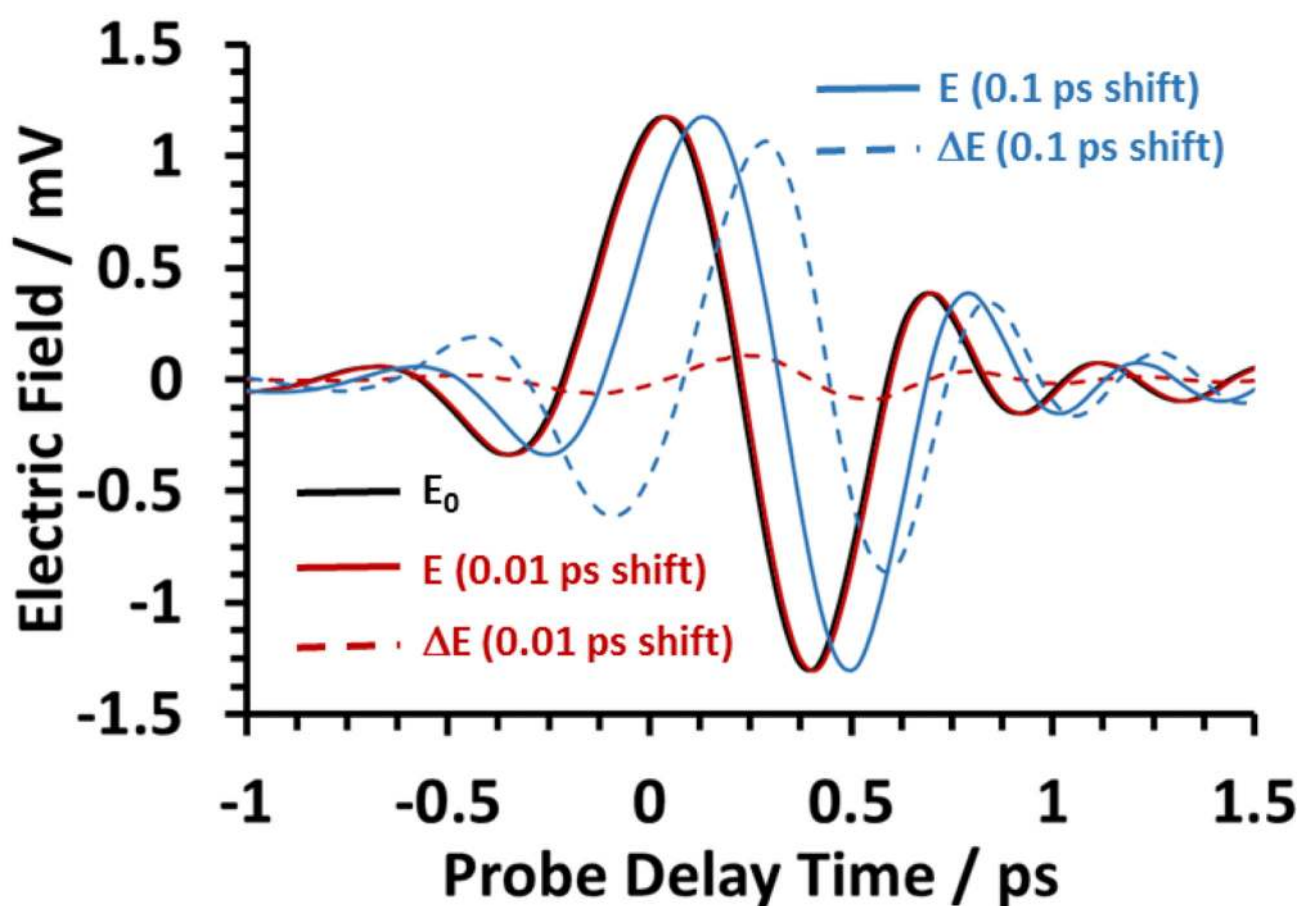
Fig. 3.
Representative THz electric field waveforms through a sample (E_0, black) compared to the same waveform arbitrarily shifted to a 0.01 ps phase delay (E, red line) and 0.1 ps phase delay (E, blue line) and the corresponding $\Delta E = E - E_0$ (dashed lines).
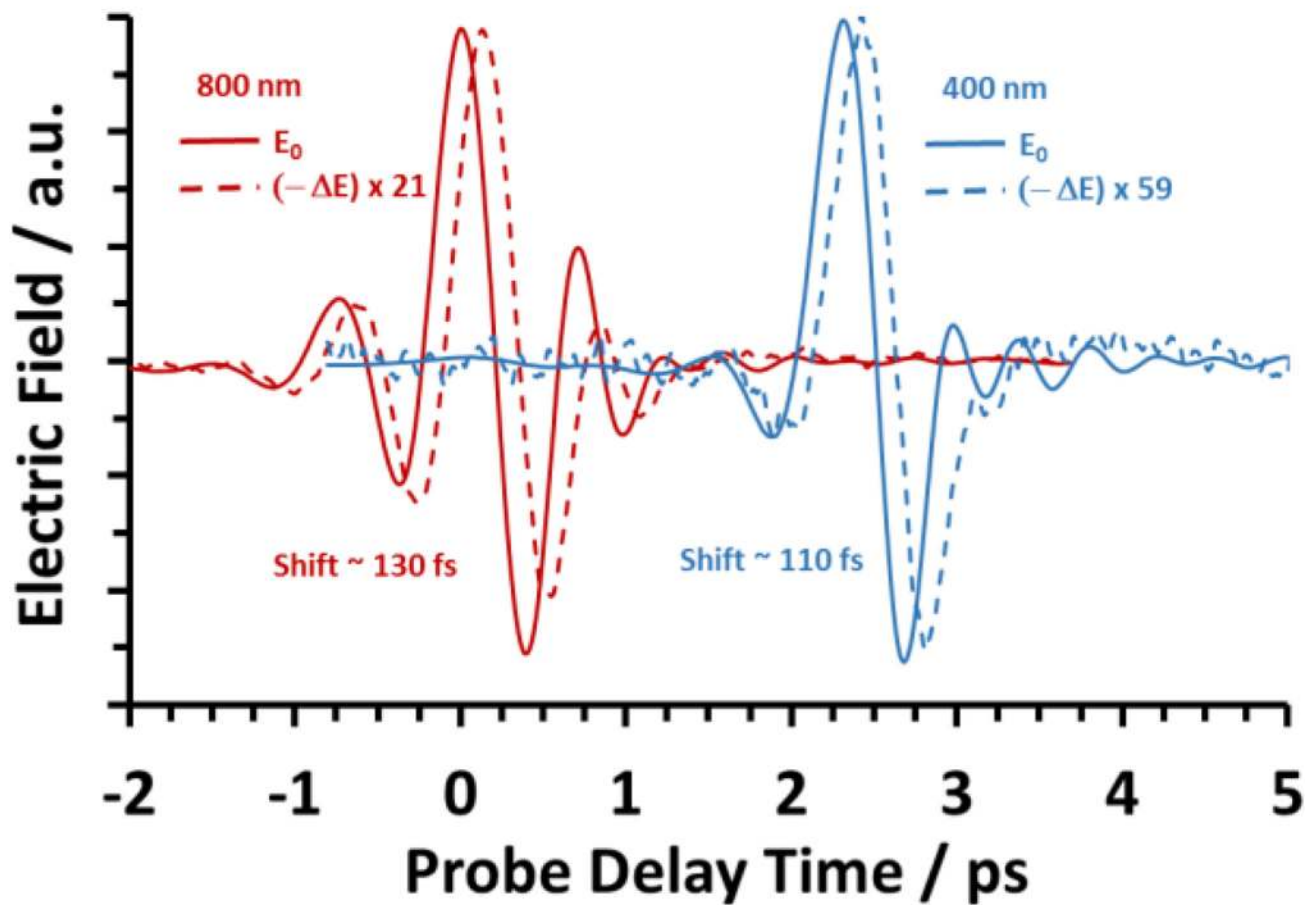
Fig. 4.
TRTS electric field waveforms transmitted through the unexcited undoped Si wafer (solid line) compared to the ΔE waveform (dashed line) transmitted 50 ps following 800 nm (red) and 400 nm (blue) excitation at approximately 1 μJ/cm^2. The ΔE waveforms have been scaled by the indicated factor relative to their corresponding E_0 and offset along the probe delay time axis for clarity.
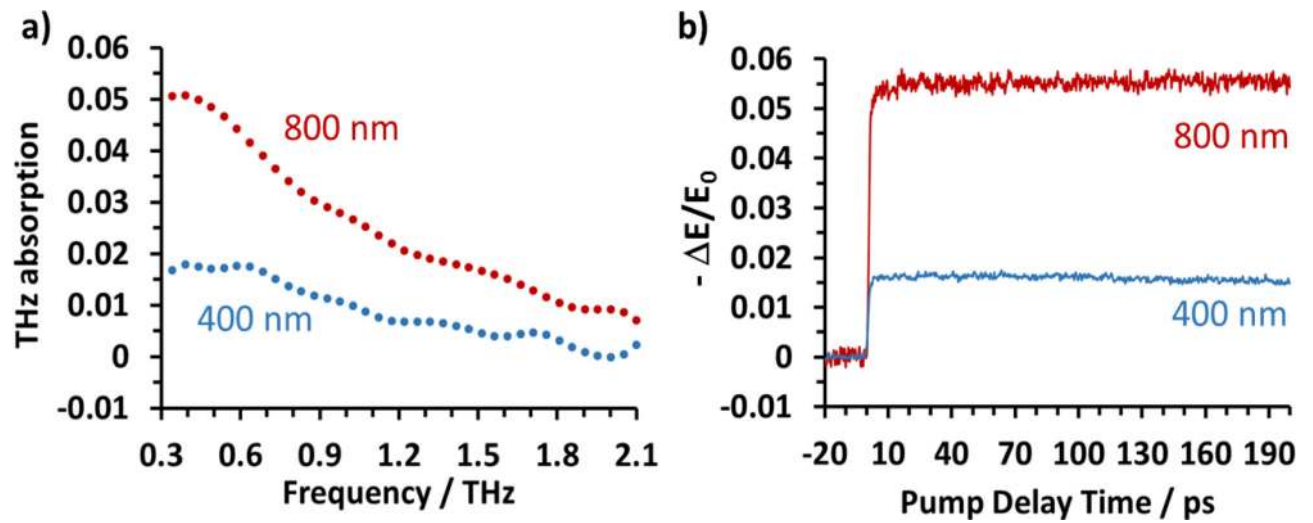
Fig. 5.

A comparison of (a) TRTS absorption spectra at 50 ps delay and (b) TRTS dynamics measured at the peak of ΔE relative to E_0 peak following photoexcitation of undoped Si at 400 nm (blue) and 800 nm (red) with approximately 1 $\mu J/cm^2$ excitation power.
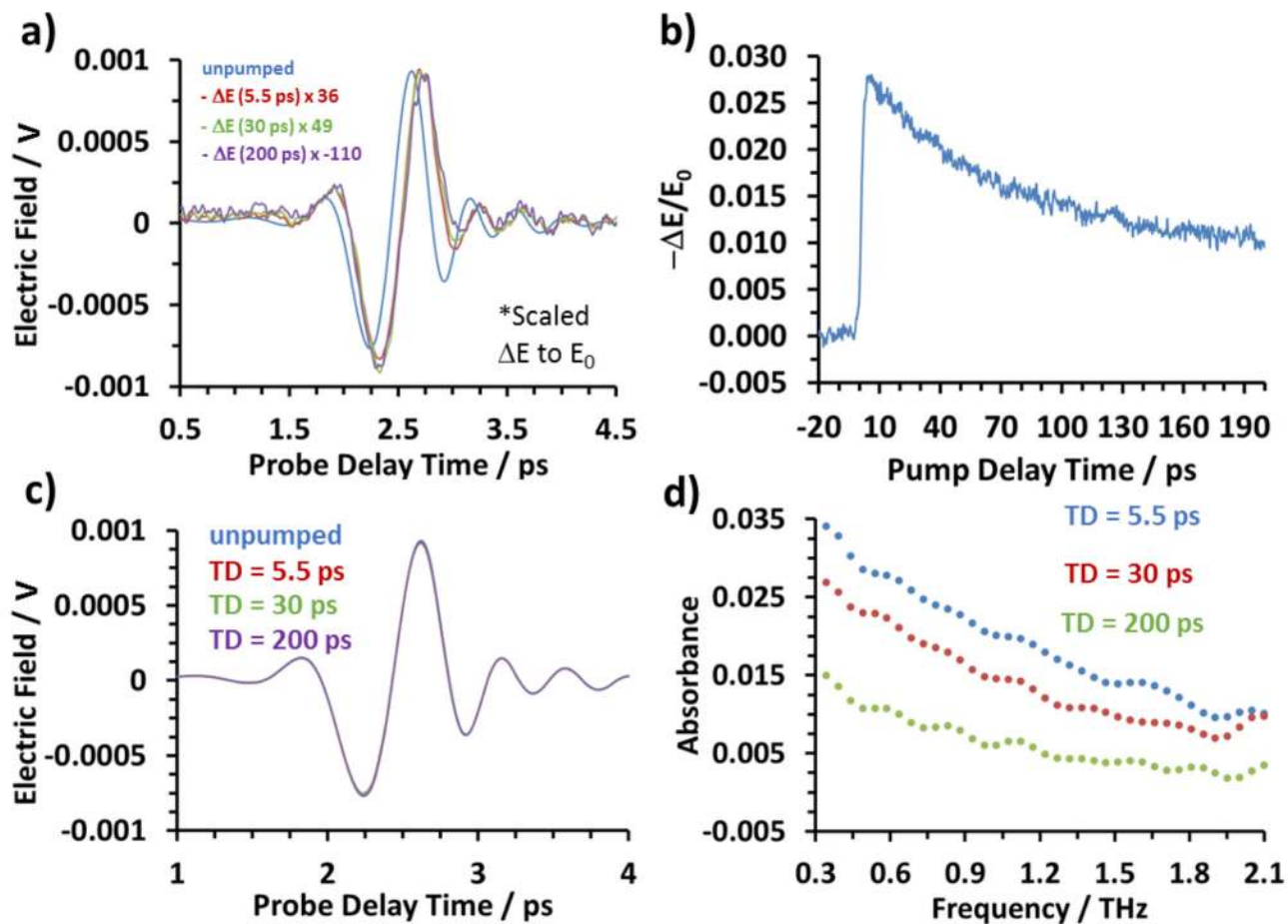
Fig. 6.
TRTS results for an undoped GaAs wafer following 400 nm excitation with 1.2 μJ/cm^2 pump power at room temperature. (a) −ΔE measured at various pump delay times compared to E_0. (b) Decay dynamics measured at the peak of ΔE which are associated with the free carrier recombination lifetime expected to be observed in this direct gap semiconductor during our 200 ps time window. (c) THz E-field transmitted through photoexcited sample determined from ΔE = E_p − E_0. The photoinduced changes are less than 3 % of E_0, and therefore E_p at each delay is basically superimposable with E_0. (d) THz transient absorption spectra determined from FFT of the waveforms shown in part (c).
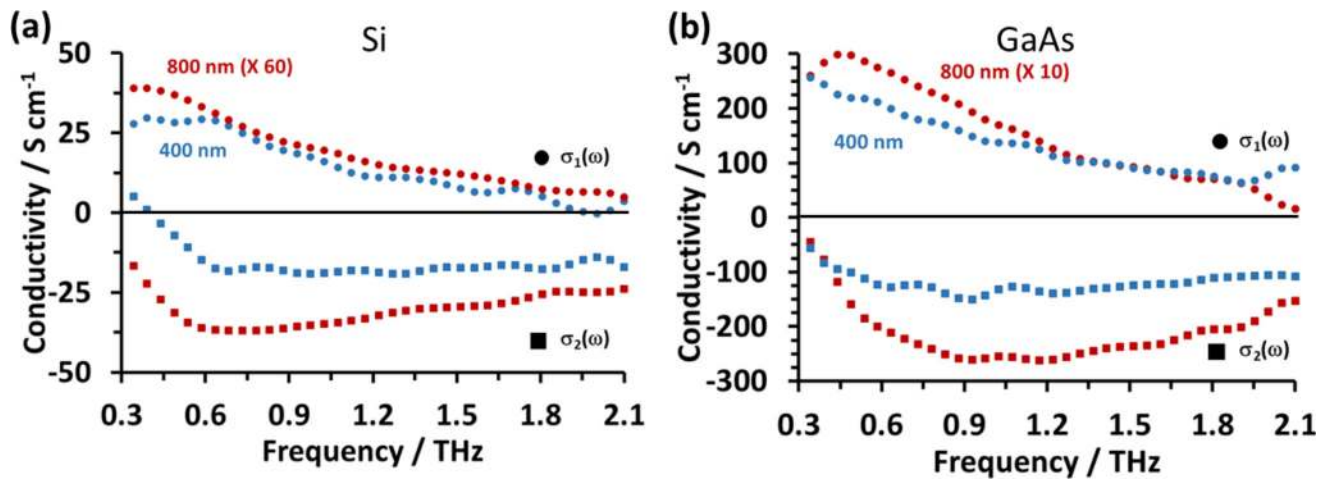
Fig. 7.
TRTS Frequency-Dependent real, $\sigma_1(\omega)$, and imaginary, $\sigma_2(\omega)$, conductivity determined by measurement of ΔE and E_0 for (a) the undoped Si wafer and (b) the undoped GaAs wafer. Both measurements obtained at room temperature and at 50 ps pump-probe delay following photoexcitation at 400 nm (blue) and 800 nm (red) with 1 $\mu J/cm^2$ incident pump power. The data with 800 nm excitation has been scaled by a factor of 60 in part (a) and a factor of 10 in part (b) for clarity.
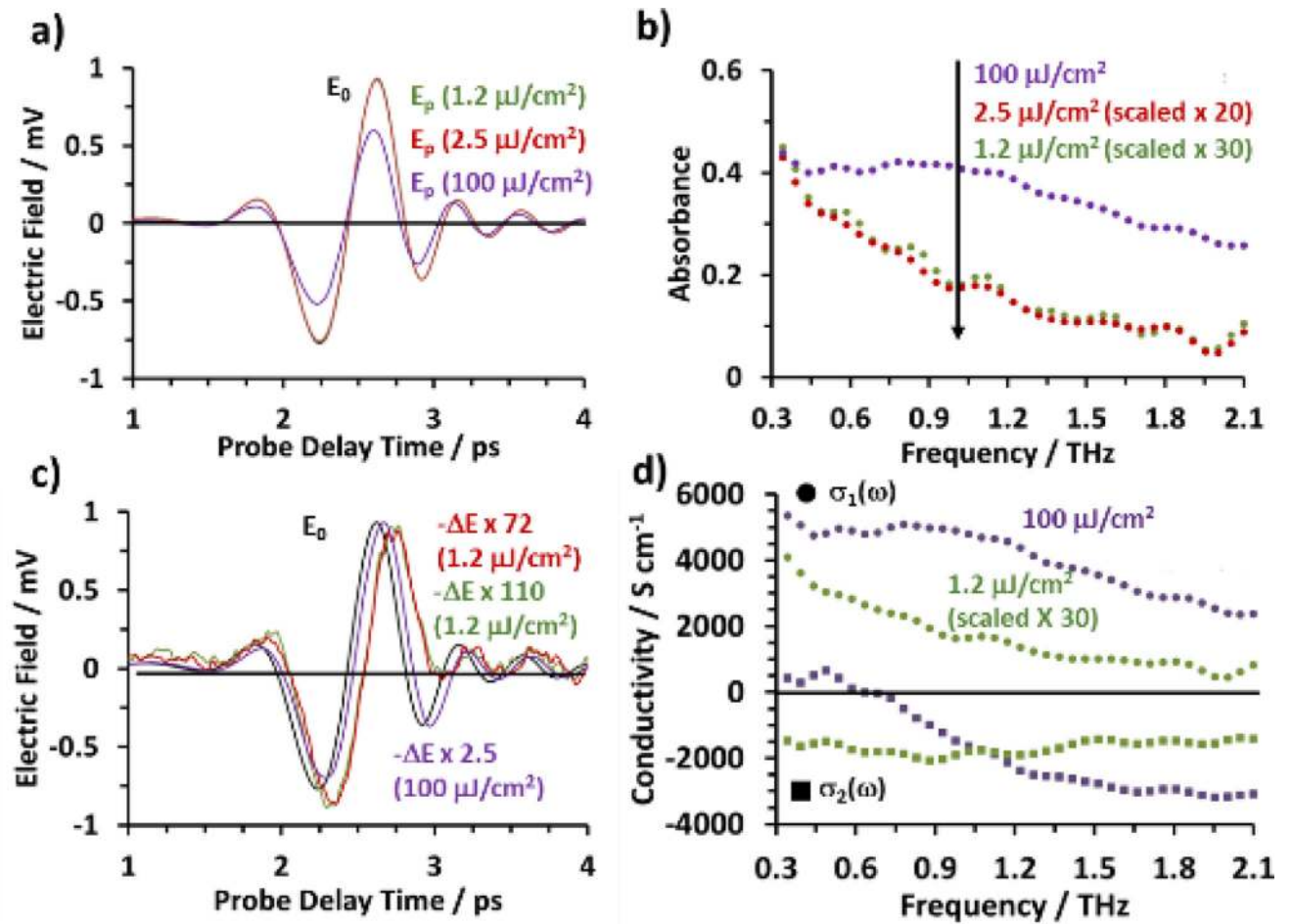
Fig. 8.
Power dependence of TRTS results for the undoped GaAs wafer following 400 nm excitation and collected at 50 ps pump time delay. Data have been collected at various excitation power ranging from 1 $\mu J/cm^2$ to 100 $\mu J/cm^2$ and scaled for aid of visualization where indicated. (a) comparison of E_p to E_0. (b) transient absorption spectra at various excitation power. (c) comparison of ΔE to E_0. (d) complex conductivity spectra determined by equation (3). The imaginary part of the conductivity in (d) is trending towards more positive values as the excitation power is increased.
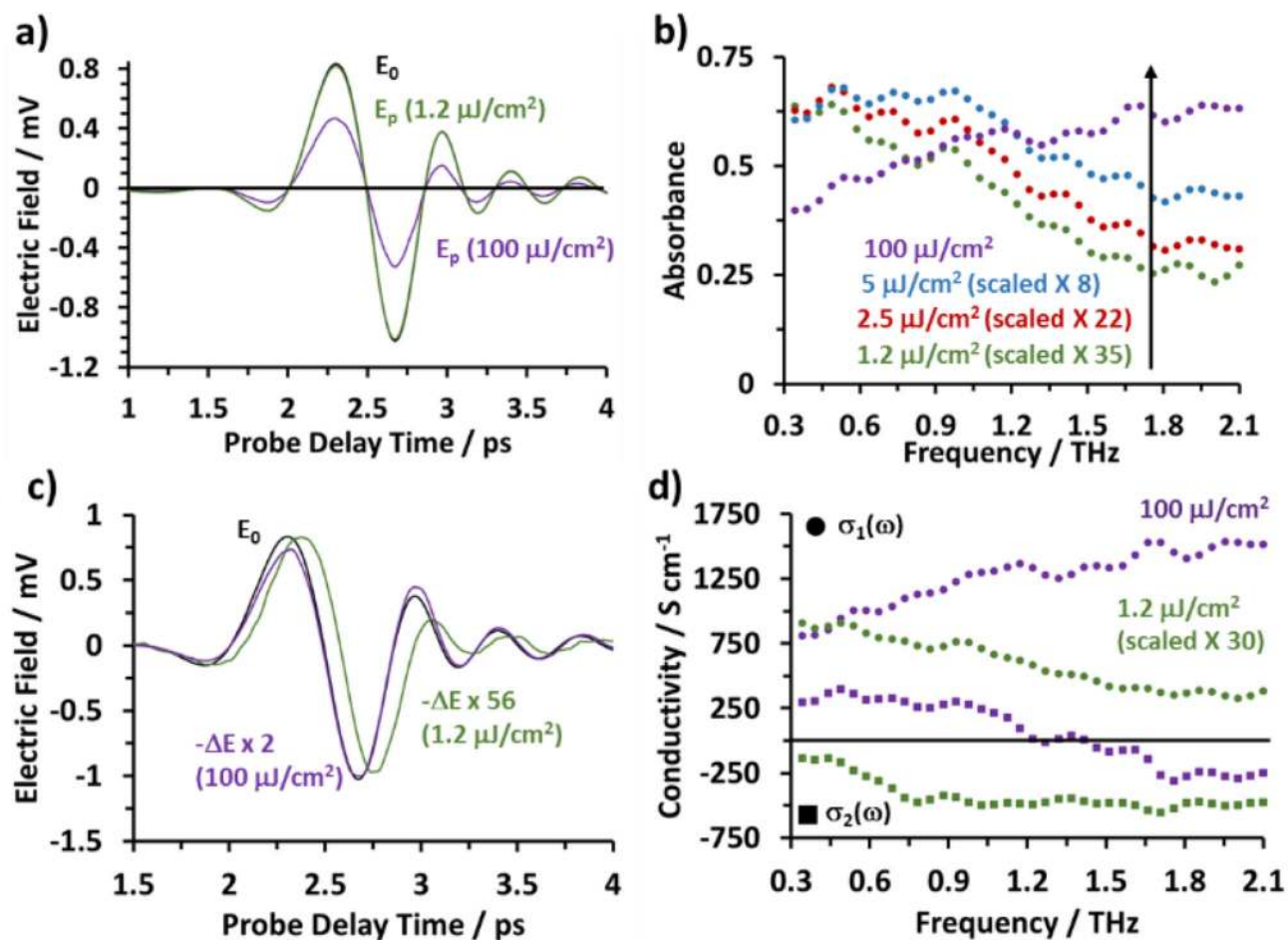
Fig. 9.
Excitation power dependence from TRTS results for the undoped Si wafer following 400 nm excitation and collected at 50 ps pump time delay. Data were collected at various excitation powers ranging from 1 μJ/cm^2 to 100 μJ/cm^2 and scaled to aid visualization where indicated. (a) comparison of E_p to E_0. (b) transient absorption spectra at selected excitation powers. (c) comparison of ΔE to E_0. (d) complex conductivity spectra determined from equation (3).
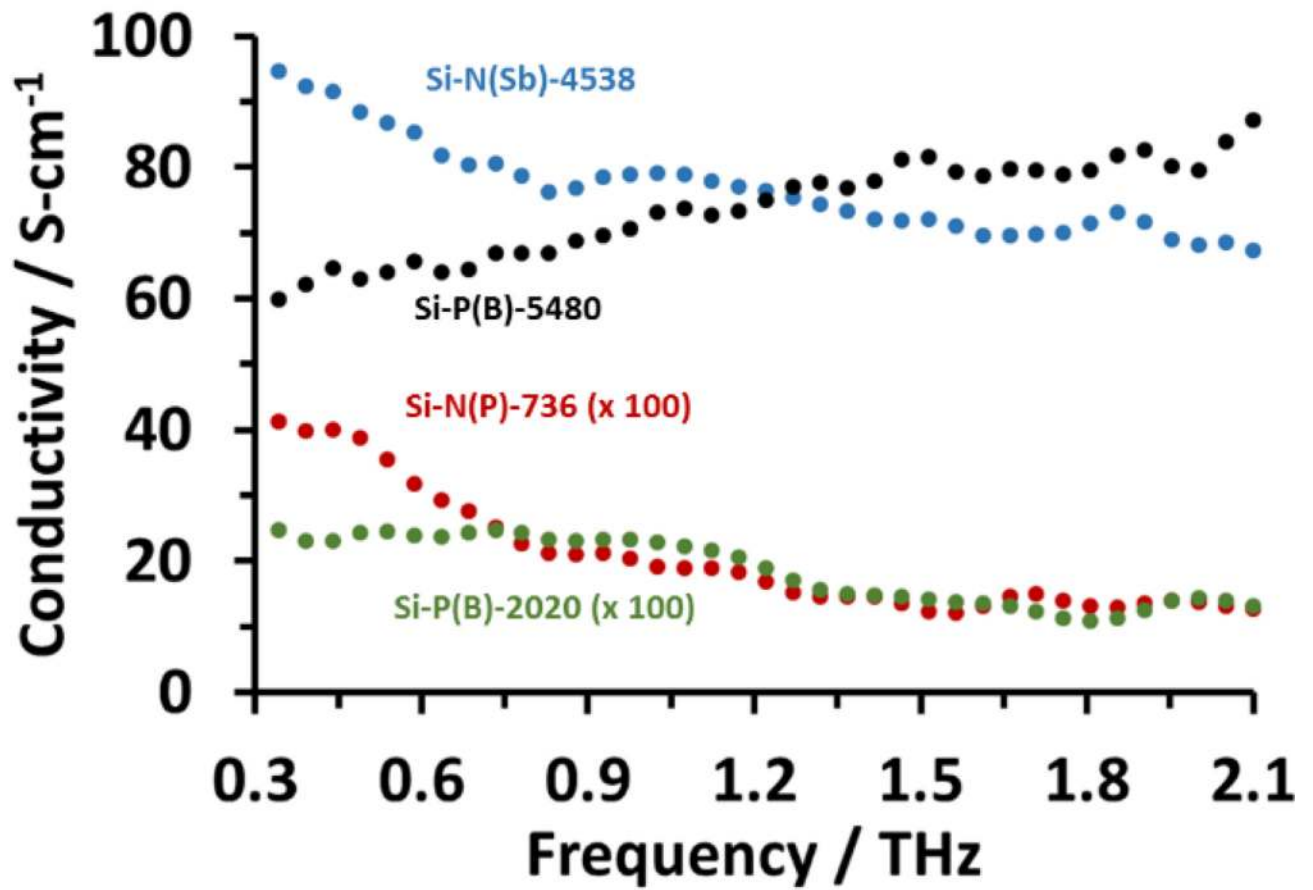
Fig. 10.
Frequency-dependent THz-TDS measurements of the real part of the conductivity for the
lightly doped (Si-N(P)-736 and Si(P(B)-2020; scaled by a factor of 100 for clarity) and
highly doped (Si-N(Sb)-4538 and Si-P(B)-5480) silicon samples at room temperature.
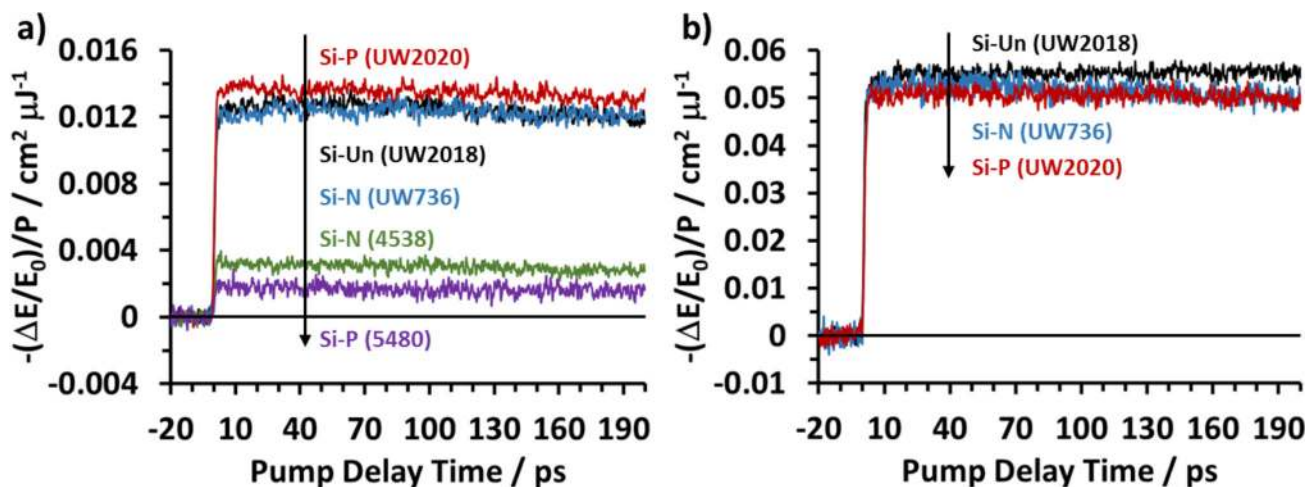
Fig. 11.
TRTS measurements at room temperature of the Silicon samples following (a) 400 nm excitation at 1.25 μJ/cm^2 (undoped, UW2018; N-type lightly doped, UW736; P-type lightly doped, UW736) and 4.75 μJ/cm^2 (highly doped N-type, lot 4538, and P-type, lot 5480). (b) The time-dependence for undoped and lightly doped silicon samples with 800 nm excitation at 1.0 μJ/cm^2. The TRTS signal magnitudes have been scaled to excitation power.
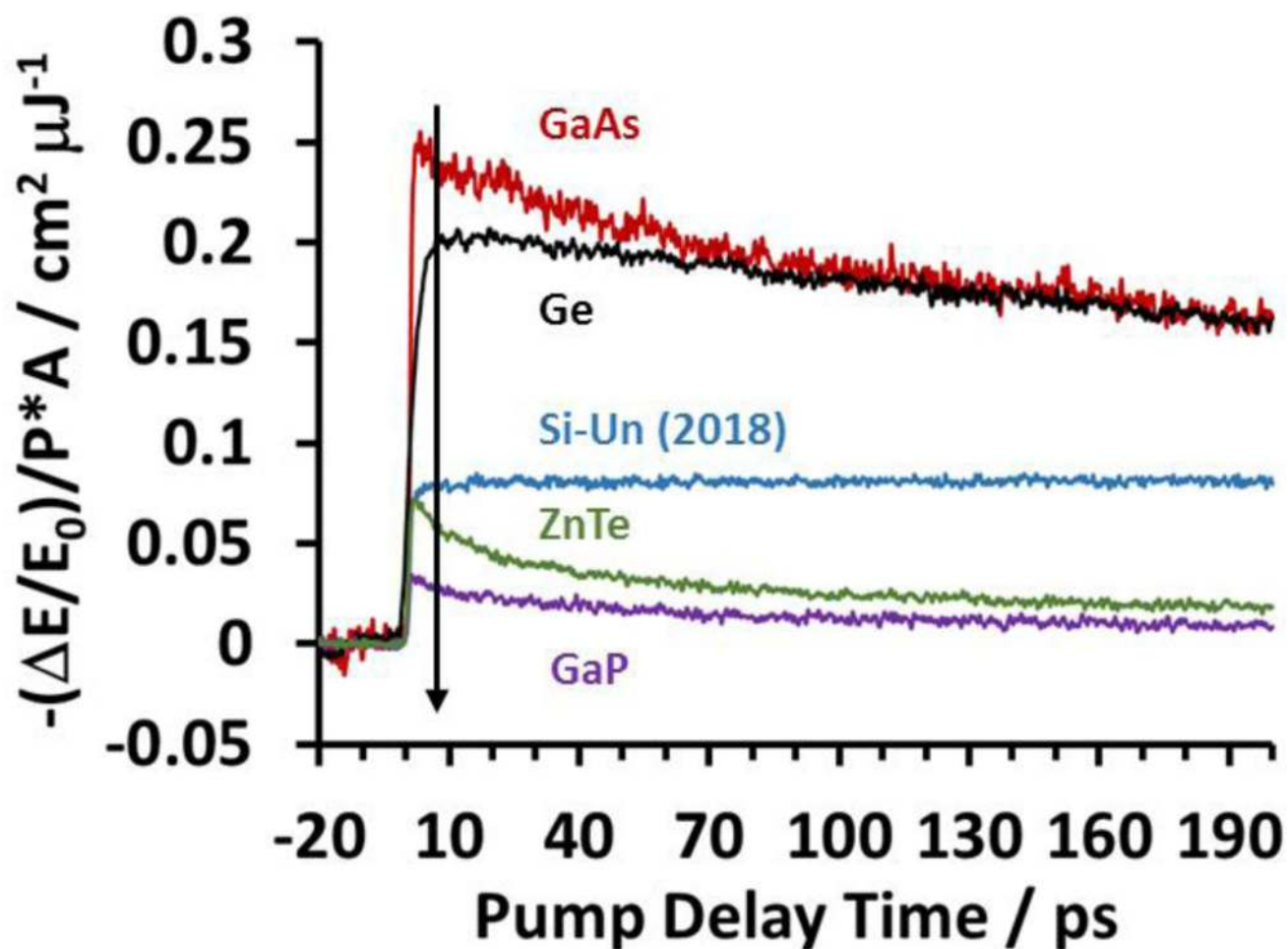
Fig. 12.
TRTS time-dependent measurements of various semiconductor samples following excitation at the following wavelengths and fluence:. Si-FZ (800 nm, 1.0 μJ/cm^2), GaAs (800 nm, 0.5 μJ/cm^2), Ge (800 nm, 0.5 μJ/cm^2), GaP (400 nm, 3.2 μJ/cm^2), and ZnTe (400 nm, 2.2 μJ/cm^2). The TRTS signal magnitudes are scaled to the same incident excitation power.

Table 1

Summary of bulk semiconductors studied and their characteristics as received from commercial sources [31]

I.D.	Material	Type[a] (Dopant)	Polish[b]	Thickness (μm)[c]	Resistivity (Ω·cm)[c]
UW2018	Si	Un	DSP	280	> 10,000
UW736	Si	N (P)	SSP	275	(1 to 10)
UW2020	Si	P (B)	DSP	280	(1 to 10)
UD8756	Si	N (Sb)	DSP	4 ± 0.5	(0.01 to 0.02)
UD9524	Si	P (B)	DSP	7 ± 0.5	(0.01 to 0.02)
WV4234	GaAs	Un	DSP	300 ± 20	N.A.
	Ge	Un	DSP	500	(53.3 to 57.9)
	GaP	Un	Crystal	500	N.A.
	ZnTe	p-type	Crystal	1000	N.A.

[a]Un = undoped, N = N-type, P = P-type, (P) = phosphorous, (B) = Boron, (Sb) = Antimony

[b]DSP and SSP stands for double-side and single-side polish, respectively

[c]Estimated thickness and resistivity quoted by the commercial provider

Table 2

Summary of THz-TDS and Van der Pauw Hall measurements of conductivity for the variously doped silicon samples

Sample	Thickness (μm)	THz-TDS		Resistivity/Hall Voltage[e]	
		σ_{dc} (S/cm)[c]	σ_{avg} (S/cm)[d]	σ (S/cm)	N (cm^{-3})
Si-Un-2018	277 ± 7[a]	N.A.	N.A.	8.3×10^{-5}	3.3×10^{11}
Si-N(P)-736	274 ± 3[a]	0.41	0.21	0.32	1.3×10^{15}
Si-P(B)-2020	282 ± 3[a]	0.25	0.19	0.17	3.0×10^{15}
Si-N(Sb)-4538	4.0 ± 0.5[b]	90	76.3	57.1	1.2×10^{18}
Si-P(B)-5480	7.0 ± 0.5[b]	65	73.8	65.4	5.4×10^{18}

[a] Average and standard deviation of multiple micrometer measurements

[b] Given by commercial provider

[c] Value at lowest measured frequency as an approximation to the DC limit

[d] Frequency-averaged conductivity between 0.4 THz to 2.0 THz

[e] accurate to ≈ 5 % uncertainty (k=1 analysis)

Table 3

Summary of TRTS data for silicon samples at various excitation wavelengths and excitation fluences

Sample	Power (μJ/cm²)	Fluence (phot/cm²)	Absorbed Density[a] (phot/cm²)	Carrier Density[b] (cm⁻³)	ΔE (V)	ΔE/E₀	Δσ (S/cm)	mobility (cm²/V·s)
Si-Un-2018 400 nm excitation	0.32	6.41E+11	3.31E+11	4.02E+16	2.79E-06	0.005	6.7	1041
	0.64	1.28E+12	6.61E+11	8.04E+16	5.22E-06	0.009	12.6	977
	0.95	1.92E+12	9.92E+11	1.21E+17	7.02E-06	0.012	17.0	879
	1.27	2.56E+12	1.32E+12	1.61E+17	9.21E-06	0.015	22.3	868
	1.59	3.20E+12	1.65E+12	2.01E+17	1.28E-05	0.021	31.3	972
Si-N-736 400 nm excitation	0.64	1.28E+12	6.61E+11	8.04E+16	4.36E-06	0.009	12.9	1002
	0.95	1.92E+12	9.92E+11	1.21E+17	6.16E-06	0.013	18.3	950
	1.27	2.56E+12	1.32E+12	1.61E+17	7.68E-06	0.016	23.0	893
	1.59	3.20E+12	1.65E+12	2.01E+17	8.70E-06	0.018	26.1	810
Si-P-2020 400 nm excitation	0.64	1.28E+12	6.61E+11	8.04E+16	5.17E-06	0.009	13.6	1039
	0.95	1.92E+12	9.92E+11	1.21E+17	7.49E-06	0.013	19.6	1009
	1.27	2.56E+12	1.32E+12	1.61E+17	9.63E-06	0.017	25.3	977
	1.59	3.20E+12	1.65E+12	2.01E+17	1.38E-05	0.025	36.4	1125
Si-N-4538 400 nm excitation	2.39	4.80E+12	2.48E+12	3.01E+17	1.14E-06	0.007	10.8	225
	4.77	9.61E+12	4.96E+12	6.03E+17	2.11E-06	0.013	20.1	209
	9.55	1.92E+13	9.92E+12	1.21E+18	4.91E-06	0.031	47.7	247
	14.32	2.88E+13	1.49E+13	1.81E+18	7.00E-06	0.044	69.0	239
	19.10	3.84E+13	1.98E+13	2.41E+18	8.69E-06	0.055	86.7	225
Si-P-5480 400 nm excitation	2.39	4.80E+12	2.48E+12	3.01E+17	6.14E-07	0.006	8.3	173
	4.77	9.61E+12	4.96E+12	6.03E+17	1.48E-06	0.013	20.2	210
	9.55	1.92E+13	9.92E+12	1.21E+18	2.12E-06	0.019	29.2	151
	14.32	2.88E+13	1.49E+13	1.81E+18	3.55E-06	0.032	49.3	170
	19.10	3.84E+13	1.98E+13	2.41E+18	4.54E-06	0.041	63.7	165
Si-un-2018 800 nm excitation	1.02	4.10E+12	2.75E+12	2.58E+15	2.67E-05	0.055	0.64	1555

Sample	Power (µJ/cm²)	Fluence (phot/cm²)	Absorbed Density[a] (phot/cm²)	Carrier Density[b] (cm^{-3})	ΔE (V)	$\Delta E/E_0$	$\Delta\sigma$ (S/cm)	mobility (cm²/V·s)
	2.04	8.20E+12	5.50E+12	5.15E+15	5.06E−05	0.105	1.29	1559
	4.07	1.64E+13	1.10E+13	1.03E+16	8.76E−05	0.181	2.43	1475
	6.11	2.46E+13	1.65E+13	1.55E+16	1.22E−04	0.252	3.69	1494
	0.51	2.05E+12	1.38E+12	1.29E+15	1.15E−05	0.026	0.30	1432
	1.02	4.10E+12	2.75E+12	2.58E+15	2.32E−05	0.052	0.61	1485
Si-N-736 800 nm excitation	2.04	8.20E+12	5.50E+12	5.15E+15	4.68E−05	0.104	1.31	1586
	3.06	1.23E+13	8.25E+12	7.73E+15	5.82E−05	0.130	1.68	1355
	4.07	1.64E+13	1.10E+13	1.03E+16	7.41E−05	0.165	2.22	1347
	0.51	2.05E+12	1.38E+12	1.29E+15	1.14E−05	0.025	0.30	1436
	1.02	4.10E+12	2.75E+12	2.58E+15	2.30E−05	0.051	0.55	1340
Si-P-2020 800 nm excitation	2.04	8.20E+12	5.50E+12	5.15E+15	4.38E−05	0.096	1.22	1484
	3.06	1.23E+13	8.25E+12	7.73E+15	6.28E−05	0.138	1.84	1489
	4.07	1.64E+13	1.10E+13	1.03E+16	8.27E−05	0.182	2.56	1552

[a]The absorbed density is the fraction of photons absorbed from the incident fluence, where the absorbance is given by 1−R, and R is the reflectivity at the pump wavelength. For 400 nm excitation, R = 0.48, and for 800 nm excitation R = 0.33, as determined from the Fresnel equation for Silicon.

[b]The carrier density is given by the absorbed density divided by the penetration depth. For 400 nm, the penetration depth is ≈ 82 nm and for 800 nm the penetration depth is ≈ 10.7 µm.

Table 4

TRTS results for each silicon wafer averaged over multiple excitation fluences compared to Hall Van der Pauw measurements on the same samples and comparable literature values.

sample	λ_{ex}	Avg pump power (μJ/cm^2)	[b]ΔN_{avg} (cm^{-3})	μ_{Avg} (cm^2/V·s)	μ (cm^2/V·s)	[c]N (cm^{-3})	μ_e (cm^2/V·s)	μ_h (cm^2/V·s)
			[a]**TRTS**		**Hall**		**Literature**[d]	
Si-Un (UW2018)	400	0.95	1.2×10^{17}	948 ± 73	1561 ± 78	1.2×10^{17}	677	304
Si-N (UW736)	400	1.11	1.4×10^{17}	914 ± 82	1538 ± 77	1.4×10^{17}	641	293
Si-P (UW2020)	400	1.11	1.4×10^{17}	1038 ± 64	352 ± 18	1.4×10^{17}	641	293
Si-N (Lot 4538)	400	10.03	1.3×10^{18}	229 ± 15	294 ± 15	2.5×10^{18}	186	108
Si-P (Lot 5480)	400	10.03	1.3×10^{18}	174 ± 22	75 ± 4	6.7×10^{18}	129	78
Si-Un (UW2018)	800	3.31	8.4×10^{15}	1521 ± 43	1561 ± 78	8.4×10^{15}	1206	434
Si-N (UW736)	800	2.14	5.4×10^{15}	1441 ± 99	1538 ± 77	6.7×10^{15}	1233	438
Si-P (UW2020)	800	2.14	5.4×10^{15}	1460 ± 79	352 ± 18	8.4×10^{15}	1206	434

[a]TRTS results averaged over multiple excitation fluences ranging over ≈ 1 order of magnitude.

[b]Change in carrier density generated by photoexcitation for both electrons and holes (given by pump fluence and penetration depth).

[c]Carrier densities equal to the sum of the intrinsic carriers (determined by Hall measurements) and those generated by photoexcitation were considered to determine the appropriate literature value for comparison.

[d]See [37–40]

Table 5

Summary of results for conductivity measurements of non-photoexcited semiconductors

Sample	Thickness (μm)	Hall Measurement[c]			Literature[d]	
		μ (cm²/V·s)	N (cm⁻³)	Type	μ$_e$ (cm²/V·s)	μ$_h$ (cm²/V·s)
Si-Un(2018)	277±7[a]	1561 ± 78	$3.3{\times}10^{11}$	N	1400	380
Ge	519±5[a]	873 ± 44	$1.2{\times}10^{14}$	P	3640	1900
GaAs	280±5[a]	N.A.	N.A.	N.A.	7200	200
GaP	500[b]	N.A.	N.A.	N.A.	300	150
ZnTe	1000[b]	107 ± 5	$1.3{\times}10^{15}$	P	340	100

[a] average value measured using multiple micrometers

[b] provided by commercial provider

[c] accurate to ≈ 5 % uncertainty (*k*=1 uncertainty analysis)

[d] published reference value for pure or lightly doped samples [40]

Table 6

TRTS data for various semiconductor samples at the indicated excitation wavelengths and excitation fluences

Sample	Power (µJ/cm²)	Fluence (phot/cm²)	Absorbed Density[a] (phot/cm²)	Carrier Density[b] (cm⁻³)	ΔE (V)	ΔE/E0	Δσ (S/cm)	mobility (cm²/V·s)
Si-Un-2018 400 nm Excitation	0.32	6.41E+11	3.31E+11	4.02E+16	2.79E-06	0.005	6.7	1041
	0.64	1.28E+12	6.61E+11	8.04E+16	5.22E-06	0.009	12.6	977
	0.95	1.92E+12	9.92E+11	1.21E+17	7.02E-06	0.012	17.0	879
	1.27	2.56E+12	1.32E+12	1.61E+17	9.21E-06	0.015	22.3	868
	1.59	3.20E+12	1.65E+12	2.01E+17	1.28E-05	0.021	31.3	972
Si-Un-2018 800 nm excitation	1.02	4.10E+12	2.75E+12	2.58E+15	2.67E-05	0.055	0.6	1555
	2.04	8.20E+12	5.50E+12	5.15E+15	5.06E-05	0.105	1.3	1559
	4.07	1.64E+13	1.10E+13	1.03E+16	8.76E-05	0.181	2.4	1475
	6.11	2.46E+13	1.65E+13	1.55E+16	1.22E-04	0.252	3.7	1494
GaAs-4234 800 nm excitation	0.51	2.05E+12	1.38E+12	1.83E+16	3.98E-05	0.084	14.8	5055
	1.02	4.10E+12	2.76E+12	3.66E+16	8.19E-05	0.173	33.7	5752
	2.04	8.20E+12	5.51E+12	7.31E+16	1.38E-04	0.293	66.5	5680
	3.06	1.23E+13	8.27E+12	1.10E+17	1.82E-04	0.385	100.6	5734
GaAs-4234 400 nm excitation	1.27	2.56E+12	1.55E+12	1.05E+18	2.54E-05	0.027	228.3	1363
Ge 800 nm excitation	0.10	4.10E+11	2.38E+11	1.17E+16	4.25E-06	0.009	6.2	3280
	0.25	1.02E+12	5.94E+11	2.93E+16	1.29E-05	0.028	19.0	4061
	0.51	2.05E+12	1.19E+12	5.86E+16	2.71E-05	0.059	41.4	4413
	0.76	3.07E+12	1.78E+12	8.80E+16	3.07E-05	0.067	47.2	3351
GaP-GmbH 400 nm excitation	1.59	3.20E+12	1.99E+12	8.60E+16	3.75E-06	0.007	4.0	290
	3.18	6.41E+12	3.98E+12	1.72E+17	6.46E-06	0.013	6.9	251
	4.77	9.61E+12	5.97E+12	2.58E+17	1.66E-05	0.033	18.1	438
	9.55	1.92E+13	1.19E+13	5.16E+17	2.69E-05	0.054	29.9	362
ZnTe 400 nm excitation	0.45	8.97E+11	6.10E+11	9.77E+16	2.95E-06	0.006	11.3	720
	1.34	2.69E+12	1.83E+12	2.93E+17	7.67E-06	0.016	28.9	617

Sample	Power (μJ/cm^2)	Fluence (phot/cm^2)	Absorbed Density[a] (phot/cm^2)	Carrier Density[b] (cm^{-3})	ΔE (V)	$\Delta E/E0$	$\Delta\sigma$ (S/cm)	mobility (cm^2/V·s)
	2.23	4.48E+12	3.05E+12	4.88E+17	1.04E−05	0.022	39.5	505
	3.12	6.28E+12	4.27E+12	6.84E+17	1.48E−05	0.031	56.5	517
	4.46	8.97E+12	6.10E+12	9.77E+17	1.90E−05	0.039	72.9	466

[a]The absorbed density is the fraction of photons absorbed from the incident fluence, where the absorbance is given by 1-R, and R is the reflectivity at the pump wavelength. Values for reflectivity at the excitation wavelength are given for each semiconductor in Table 7.

[b]The carrier density is given by the absorbed density divided by the penetration depth. The details used to calculate this are given in Table 7.

Table 7

Tabulated parameters needed to determine carrier density from photoexcitation in TRTS experiments

Sample	Excitation Wavelength (nm)	Absorption Coefficient[a] (cm⁻¹)	Penetration Depth[a] (μm)	% R[b]
Si-Un-2018	400	121 580	0.082	0.48
Si-Un-2018	800	937	10.7	0.33
GaAs-4234	400	674 185	0.015	0.39
GaAs-4234	800	13 267	0.75	0.33
Ge	800	49 323	0.20	0.42
GaP-GmbH	400	43 200	0.23	0.38
ZnTe	400	160 000	0.063	0.32

[a]
For ZnTe see [41]. For the other samples see [32].

[b]
Percent reflectivity at the visible excitation wavelength was determined for each sample using the Fresnel equation. See [32].

Table 8

TRTS results for each semiconductor sample averaged over multiple excitation fluences compared to Hall Van der Pauw measurements and literature values.

Sample	λ_{ex} (nm)	TRTS			Hall		Literature[a]		
		Avg Pump Power (μJ/cm^2)	ΔN_{Avg} (cm^{-3})	μ_{Avg} (cm^2/V·s)	μ (cm^2/V·s)	N (cm^{-3})	μ_e (cm^2/V·s)	μ_h (cm^2/V·s)	
Si-Un-2018	400	0.95	1.2×10^{17}	948 ± 73	1561 ± 78	1.2×10^{17}	677	304	
Si-Un-2018	800	3.31	8.4×10^{15}	1521 ± 43	1561 ± 78	8.4×10^{15}	1206	434	
GaAs-4234[b]	400	1.27	1.1×10^{18}	1363	N.A.	1×10^{18}	2700	150	
GaAs-4234	800	1.66	5.9×10^{16}	5555 ± 334	N.A.	6×10^{16}	5000	375	
Ge	800	0.41	4.7×10^{16}	3776 ± 552	873 ± 44	5×10^{16}	2100	1500	
GaP	400	4.77	2.6×10^{17}	335 ± 83	N.A.	2.5×10^{17}	160	120	
ZnTe	400	2.32	5.1×10^{17}	565 ± 103	107 ± 5	N.A.	N.A.	N.A.	

[a] Literature values given for room temperature measurement at a carrier density equivalent to ΔN from TRTS. Literature data obtained for Si [39], GaAs [42–44], Ge [44–46], GaP [44,47]. For ZnTe literature data is limited [48] and could not be found for the TRTS experimental carrier density.

[b] This experiment was performed at a single excitation power.